

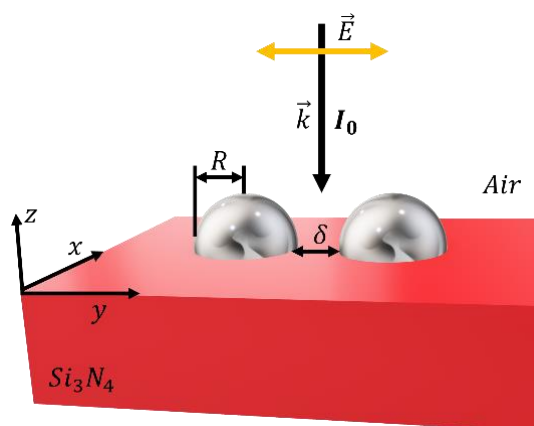


Active Optical Phase-Change Plasmonic Transdimensional Systems  
Enabling Femtojoule and Femtosecond Extreme Broadband Adaptive  
Reconfigurable Devices

Grant Agreement No: 899598

Deliverable D2.2

# Electromagnetic Study of Behaviour of Plasmonic Units



Deliverable type:	Report
Deliverable reference number:	899598 / D2.2 / v.1.0
Deliverable title:	Electromagnetic Study of Behaviour of Plasmonic Units
WP contributing to the deliverable:	WP2
Dissemination level	Public
Responsible Editor:	UC
Due date:	31/05/2021 (M12)
Actual submission date:	31/05/2021 (M12)

Start of the Project: June 1 <sup>st</sup> , 2020	Duration: 36 months
Coordinator: Maria Losurdo, CNR-NANOTEC	Contact: maria.losurdo@cnr.it coordinator@phemtronics.eu
Project website	www.phemtronics.eu

## Authors List

Organization	Author(s)
UC	Prof. Fernando Moreno Dr. Pablo Albella Prof. Francisco Gonzalez Prof. José M <sup>a</sup> Saiz Gonzalo Santos
CNR	Dr. Maria Losurdo, Dr. Yael Gutiérrez

## Log of changes






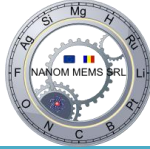


Version

V1.0

Changes

Document created 31/05/2021

## Members of the PHEMTRONICS Consortium

	Istituto di Nanotecnologia Consiglio Nazionale delle Ricerche Via Amendola 12/D 70126 Bari, Italy <a href="http://www.nanotec.cnr.it">www.nanotec.cnr.it</a>	<b>Project Coordinator:</b> <b>Maria Losurdo</b> <a href="mailto:maria.losurdo@cnr.it">maria.losurdo@cnr.it</a> <a href="mailto:coordinator@phemtronics.eu">coordinator@phemtronics.eu</a>
	Westfälische Wilhelmsuniversität Münster Schlossplatz 2, 48149 Münster, Germany <a href="http://www.uni-muenster.de/en/">www.uni-muenster.de/en/</a>	<b>Prof. Wolfram Pernice</b> <a href="mailto:wolfram.pernice@uni-muenster.de">wolfram.pernice@uni-muenster.de</a>
	University College Cork - National University Of Ireland, 1 Dyke Parade, Cork, T12 FE00, Ireland <a href="http://www.tyndall.ie">www.tyndall.ie</a>	<b>Dr. Mircea Modreanu</b> <a href="mailto:mircea.modreanu@tyndall.ie">mircea.modreanu@tyndall.ie</a>
	Johannes Kepler University Altenbergerstraße 69, 4040 Linz, Austria <a href="http://www.jku.at/en/">www.jku.at/en/</a>	<b>Dr. Christoph Cobet</b> <a href="mailto:Christoph.Cobet@jku.at">Christoph.Cobet@jku.at</a>
	University of Cantabria Avda. Los Castros s/n Santander, 39005, Cantabria, Spain <a href="http://www.unican.es">www.unican.es</a>	<b>Prof. Fernando Moreno</b> <a href="mailto:fernando.moreno@unican.es">fernando.moreno@unican.es</a>
	NANOM MEMS SRL Strada George Coșbuc 9 Râșnov 505400 Brașov, Romania <a href="http://www.nanom-mems.com">www.nanom-mems.com</a>	<b>Dr. Marin Gheorghe</b> <a href="mailto:maringhe@nanom-mems.com">maringhe@nanom-mems.com</a>
	TE-OX Parc Orsay Université 2 Rue Jean Rostand 91893 Orsay Cedex France <a href="http://www.te-ox.com">www.te-ox.com</a>	<b>Dr. Guy Garry</b> <a href="mailto:guy.garry@te-ox.com">guy.garry@te-ox.com</a>
	VLC PHOTONICS SOCIEDAD LIMITADA Building 9B , Office 0.71 Universidad Politécnica de Valencia Camino de Vera s/n, 46022 Valencia, Spain <a href="http://www.vlcphotonics.com">www.vlcphotonics.com</a>	<b>Dr. Jordi Soler</b> <a href="mailto:jordi.soler@vlcphotonics.com">jordi.soler@vlcphotonics.com</a>

## About Phemtronics

PHEMTRONICS was launched in June 2020 as a 3-year collaborative project on CMOS-compatible phase-change materials, plasmonic, photonic and electronic integration.

**PHEMTRONICS** aims at replacing “slow” electrical or thermal phase change materials with “ultrafast” “Optical-Phase-Change Plasmonic Materials”, capable of self-reconfiguring and self-adapting as a response to light, shifting from current technology paradigms based on electronic switching to “all-optical switching” enabling broadband reconfigurability of devices.

**PHEMTRONICS** will enable a new technology paradigm of adaptive optical signal processing with ultrafast network reconfiguration with key metrics of the “femtosecond-scale switching time”, “ultralow power of femtojoule/bit” and “microwave-to-optical frequencies” broadband capability required for reliable multibit operations. The exciting outcomes include demonstrations of:

- Ultrafast and low-power switches;
- Adaptive antennas;
- Adaptive switchable multiple-band detection for the future generation of photodetectors;
- All-optical spiking neuron circuit, with integrated all-optical synapses.

## List of Abbreviations

Ag = Silver  
Au = Gold  
FDTD = finite-difference time-domain  
FEM = finite element method  
Ga = Gallium  
GaS = Gallium Sulfide  
 $\text{Ga}_2\text{S}_3$  = Gallium Trisulfide  
GeS = Germanium Sulfide  
LO = longitudinal mode  
LSPR = Localized Surface Plasmon Resonance  
PCM = Phase Change Materials  
PDE = partial differential equations  
S, Se, Te = Chalcogenides of sulfur, selenium tellurium  
 $\text{Sb}_2\text{S}_3$  = Antimony Sulfide  
SERS = Surface Enhanced Raman Spectroscopy  
 $\text{Si}_3\text{N}_4$  = Silicon Nitride  
TO = Transverse plasmonic mode

## Table of Contents

<b>EXECUTIVE SUMMARY .....</b>	<b>6</b>
<b>INTRODUCTION.....</b>	<b>7</b>
<b>2. METHODS.....</b>	<b>10</b>
<b>3. PLASMONIC ACTUATION .....</b>	<b>10</b>
3.1 Screening of different plasmonic materials.....	10
3.2 Gallium as an alternative plasmonic metals to be coupled to chalcogenides PCMs .....	13
<b>4. PHOTOTHERMAL PLASMONICS.....</b>	<b>26</b>
<b>5. PLASMONICS VS THERMOPLASMONICS .....</b>	<b>33</b>
<b>6. CORE-SHELL RECONFIGURABLE NANOANTENNAS .....</b>	<b>35</b>
<b>7. PLASMON-COUPLING FOR RECONFIGURABLE PHOTODETECTORS .....</b>	<b>38</b>
<b>8. CROSS-CHECK WITH EXPERIMENTAL DATA ON PLASMONIC ACTUATION .....</b>	<b>44</b>
<b>9. IDENTIFIED SOLUTIONS.....</b>	<b>50</b>
<b>10. CONCLUSIONS .....</b>	<b>52</b>
<b>11. REFERENCES .....</b>	<b>52</b>

## Executive Summary

For any memory or computing device, fast switching speed and low switching energy are most attractive attributes, and approaches by which speed and energy efficiency can be improved are always desirable.

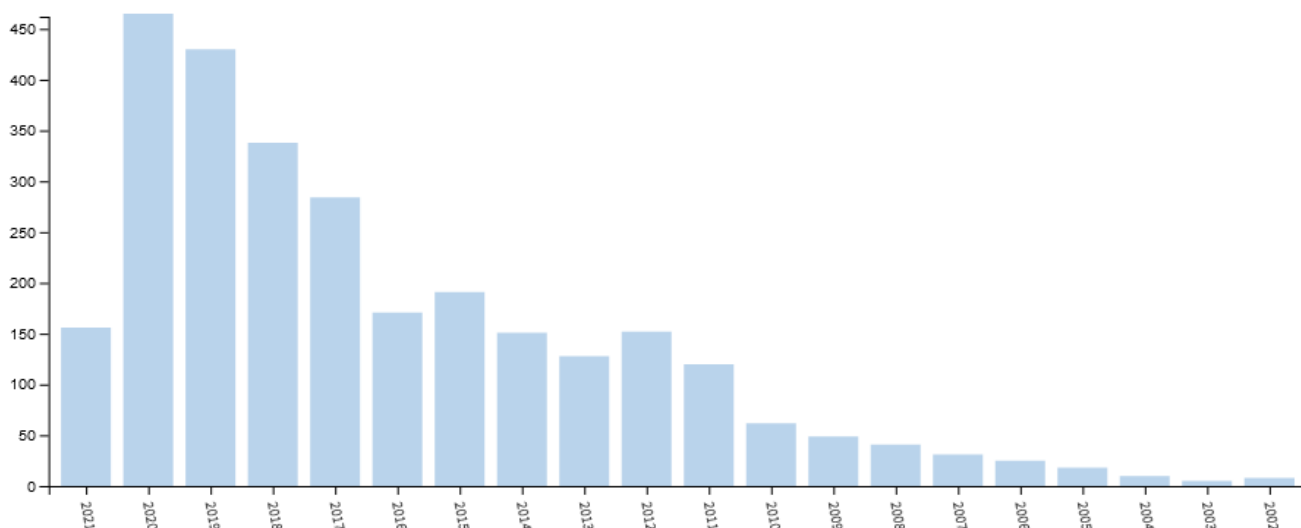
Plasmonics offers a way to achieve those attributes of fast switching and low energy consumption: plasmonic resonant structures are inherently capable of harnessing and focusing optical energy on sub-wavelength scales, far beyond the capabilities of conventional optical and photonic elements. Plasmonics can provide us with access to both of these scenarios. Indeed, plasmonics offers additional light manipulation tools, otherwise inaccessible with conventional photonics. The collective oscillation of conduction electrons in a suitably shaped metallic nanoparticle (the so-called localized surface plasmon, LSP) can couple with impinging radiation, which in turn squeezes light into much reduced volumes, and greatly magnifies the local electric field, usually leading to a much reduced (non-diffraction limited) device footprint.

This deliverable presents an analysis of the electromagnetic interaction of plasmonic units with phase-change materials (PCMs) as selected in the project PHEMTRONICS. As plasmonic units, we start by considering the common plasmonic metals of gold and silver, analyzing their possibilities and limits. Based on those, we consider the use of metallic nanoantennas made of Ga nanoparticle dimers. Ga has been selected due to its good plasmonic performance, physical and chemical properties and to its polymorphism. We have analyzed the coupling of plasmonic nanoantennas with the PCMs under consideration at the moment in the project, namely, GaS and Sb<sub>2</sub>S<sub>3</sub> in their amorphous and crystalline phases. These two PCMs have been combined with Ga NPs and some gold configurations to make the nanoantenna reconfigurability wider and improve its tunability and performance. Further, plasmon coupling to PCM waveguides made of Sb<sub>2</sub>S<sub>3</sub>, has been analyzed through metallic grating couplers. Two basic configurations have been selected which could be the base to design a plasmonic enhanced PCM photodetector in collaboration with the PHEMTRONICS partners. Finally, conclusions have been drawn together with the identification of the practical solutions to couple plasmonics with novel PCMs.

## Introduction

Plasmonics<sup>1</sup> and Thermoplasmonics<sup>2</sup> are two recent research areas which are gaining increasing attention due to the possibility to enhance light-matter interactions when metallic nanomaterials are excited by electromagnetic radiation. Plasmonics is a consequence of the collective oscillation of free electrons in metals that are confined in dimensions much smaller than the incident wavelength, usually in the UV-VIS-NIR ranges, i.e. hundreds of nanometers. This leads to several important effects, like the concentration of electromagnetic energy at the nanoscale level, the enhancement of the electromagnetic field in the proximities of the nanostructure, and its increment of temperature and consequently its surroundings due to the inherent ohmic losses in metals. Thermoplasmonics is exploited in different fields, especially in those related to the treatment of diseases, like cancer, where thermal treatments can be beneficial.<sup>2</sup> Thermal effects induced by an electromagnetic field are usually concentrated around nanostructures at a length scale of tenths of nanometers, much smaller than the exciting wavelength. Both, plasmonic and thermoplasmonic effects run in parallel when a metallic nanostructure is illuminated by electromagnetic radiation and they are concentrated at the nanoscale level. Once the electronic plasma of the nanostructure is excited, both scattering and absorption effects appear, the latter leading to thermoplasmonics effects and consequently, to the heating of the nanostructure and its surroundings at nanoscale distances.

During the last 20 years there has been a lot of attention to phase change materials (PCM), as indicated by the increasing number of papers devoted to the subject shown in Fig. 1.



**Figure 1.-** Number of papers published per year with the topic “Phase Change Materials” (Source: Web of Science)

PCMs are materials whose structure and related optical properties change when an external stimulus (electrical, optical, thermal, etc.) is applied. A striking and functional feature of the most common PCMs is the high contrast between their crystalline and amorphous phases.<sup>3,4</sup> In particular, PCMs made of chalcogenide (S, Se, Te) compounds have the ability to switch between these two states in response to appropriate heat stimuli (crystallization) or melt-quenching processes (amorphization).<sup>5</sup>

It has recently been shown that the combination of PCM and nanoplasmonics paves the way to innovative switching devices with a considerable reduction of the active volume of the PCM. This makes easier the phase transition and consequently, its response to the external stimulus.<sup>6</sup> Combining plasmonics with PCMs is a particularly promising approach for satisfying such stringent requirements, since the dimensions of such devices can be reduced to tens of nanometers and smaller—significantly below the diffraction limit of traditional optical devices. Therefore, plasmonic PCMs are attractive to achieve an increase of the switching speed and a reduction of the energy consumption needed to heat up PCMs and operate their phase transition.

The combination of high electrical conductivity and strong plasmonic resonance at optical wavelengths in silver (Ag) and gold (Au) has led to extremely compact electro-optic nanogap devices such as photodetectors and modulators<sup>7</sup>. While plasmonics permits very strong light-matter interaction in nanometer-scale devices, the relatively high loss of metals at optical frequencies makes guiding light inefficient.

For some applications, both thermal and nonthermal, i.e., hot-spots, effects can work synergistically to increase the efficiency of the phase-change process<sup>8</sup>. Basic arrangements have been presented in two different approaches where the PCM is sandwiched in a dimer plasmonic configuration<sup>8,9</sup>:

- 1) in the first, the PCM acts as direct active material by “modulating” the electromagnetic transmitted energy;
- 2) in the second, its interaction with a dielectric wave-guide changes its transmission properties through changes in the evanescent wave interaction of the PCM.

Based on those considerations, this deliverable presents a detailed analysis of the combination of PCM and plasmonic dimer nanoantennas to enable the development of fast and efficient switching devices by taking advantage of the two new PHEMTRONICS paradigms:

- 1) New options for PCMs: PHEMTRONICS surpasses the current paradigm of PCM by developing extreme broadband transparent O-PCMs that combine broadband low loss (0.4 – 18.5  $\mu\text{m}$ ) and large optical contrast ( $\Delta n \approx 2$ ) based on sulfides (GaS, Ga<sub>2</sub>S<sub>3</sub>, Sb<sub>2</sub>S<sub>3</sub>, GeS), which possess several phases, optical band gap, higher refractive indices and low phonon frequencies are attractive for applications that require high transmission from the visible to the mid-infrared<sup>10</sup> (see deliverable D2.1).



- 2) New options for nanoantennas: PHEMTRONICS surpasses the current paradigm of passive plasmonics and metamaterial structures that, after fabrication, have optical properties limited to a certain functionality or operating wavelength, like coinage metals, gold and silver. We have very recently (2019) demonstrated plasmonic gallium (Ga) nanoparticles,<sup>11</sup> with 5 possible phases, with markedly different optical properties ranging from those of an almost semiconductor-like, partially covalent solid phase to those of a highly metallic liquid, as dynamically reconfigurable nanoantennas, light induced phase-change switching and therefore active phase change plasmonics. In addition, we propose gallium as alternative to gold and silver, which show a high degree of diffusivity in chalcogenide-based compounds, with their diffusion being activated by temperature.<sup>12</sup>

This deliverable is organized as follows:

- Section 2 contains the description of the numerical methods used in all the calculations.
- Section 3 is devoted to the analysis of the coupling of light by plasmonic nanostructures into the PCM material to achieve a more efficient light absorption process to activate the phase-change. Here, as plasmonic unit, a dimer of hemispherical Ga nanoparticles on  $\text{Si}_3\text{N}_4$  has been chosen.  $\text{Si}_3\text{N}_4$  was selected to act either as a waveguiding substrate or as a substrate of a PCM based waveguide. The analysis performed in this section has been done as a function of the parameters involved in the design of the plasmonic: nanoparticle size, which in turn selects the plasmonic mode, and the gap distance in the dimer.
- Section 4 argues on the thermoplasmonic effect of the different configurations described in Sect. 3. Since metallic NPs illuminated at their plasmonic resonance can act as heat sources due to the joule losses into the material. Here we explore the possibility of taking advantage of the heat for the PCM crystallization-amorphization process.
- Section 5 establishes a comparative parallelism between both the plasmonics and thermoplasmonics effects produced in the proposed configurations to establish if both effects can be synergetically exploited to activate the phase-change process.
- Section 6 presents the design of a new concept of plasmonic phase change nanoantenna that will be investigated in PHEMTRONICS.
- Section 7 discusses the application of a plasmonic design for a possible  $\text{Sb}_2\text{S}_3$  phase-change plasmonic photodetector identified as a possible device to be implemented in the course of the project.
- Section 8 demonstrates the limits encountered experimentally in coupling conventional plasmonic metals of gold and silver with chalcogenides phase change materials.
- In light of the problems exposed in the previous section, Section 9 proposes solutions to be investigated further in the course of the project.

## 2. Methods

For electromagnetic simulations finite-difference time-domain (FDTD) simulations have been performed with Lumerical software.<sup>13</sup> FDTD belongs in the general class of grid-based differential time-domain numerical modeling methods. Maxwell's equations (in partial differential form) are modified to central-difference equations, discretized, and implemented in software.

For temperature simulations, numerical simulations based on the finite element method (FEM) have been performed in COMSOL.<sup>14</sup> FEM is used to find an approximate solution of partial differential equations (PDE) and integral equations. The solution approach is based either on eliminating the time derivatives completely (steady state problems), or rendering the PDE into an equivalent ordinary differential equation, which is then solved using standard techniques such as finite differences.

## 3. Plasmonic Actuation

### 3.1 Screening of different plasmonic materials

Previous research has studied the performance of different nanoantennas for the transformation of phase-change materials (PCMs). These nanoantennas were usually made of gold (Au) and silver (Ag).

However, we are considering that both Au and Ag may show chemical interaction (interfacial reactions, diffusion) with chalcogenide elements in the PCMs that may lead to a non-effective plasmonic enhancement. This is a drawback of Au and Ag plasmonics that most of research groups working on coupling plasmonic with PCMs have not duly considered.

Indeed, we find experimentally (see section 8) that reaction of sulfur-chalcogenides as well as selenium- and tellurium based PCMs is an issue that must be considered when designing phase change material-tuned plasmonic structures. This reaction alters the shape of the plasmonic nanoantennas and, consequently, their resonances. Furthermore, diffusion and/or reactivity can also influence the crystallization kinetics and optical constants of the phase change materials.

From a plasmonic design perspective, placing the chalcogenide directly in contact with the metal is ideal to maximize the light-matter interaction. This argument can be rationalized considering that the plasmonic effects decay exponentially with distance. The strong light-matter interaction promoted by the excitation of localized surface plasmons at the interface between the nanoantennas and the PCM allows to reduce the thickness of the PCM layer. Having all this in mind, it is important to identify plasmonic materials that can be

directly interfaced with phase change chalcogenides without inter-diffusion and/or reactivity between the metal and the PCM layers.

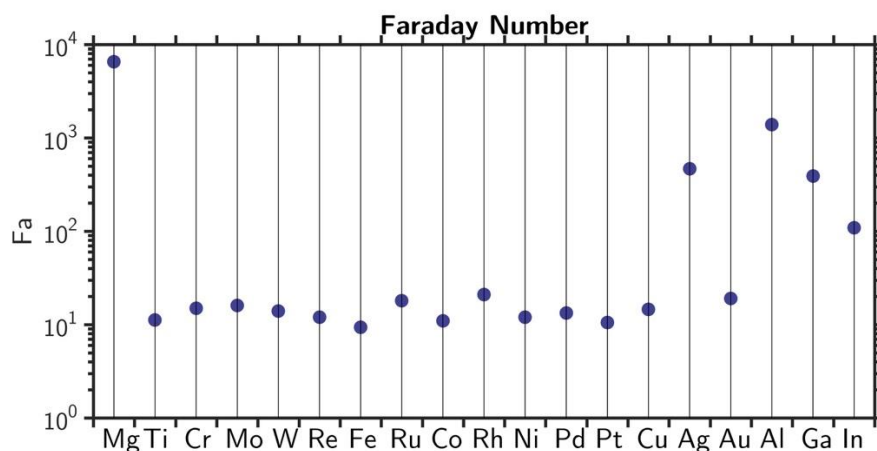
In this deliverable, we propose Gallium (Ga) as an alternative plasmonic metal to Au and Ag.

Ga has demonstrated to perform well as plasmonic metal producing high near-field enhancement showing no chemical reactivity or diffusion with the chalcogenides materials of interest in this project.

In order to give an objective proof for the potential of Ga as a plasmonic metal when compared to other conventionally used materials in plasmonics, we have calculated the Faraday number (Fa) as figure-of-merit for this comparison. This dimensionless parameter, as proposed by Lalisie et al.<sup>15</sup>, quantifies the ability of a nanoparticle to enhance the electric field intensity in its surrounding medium. For simplicity, we consider the Faraday number for the case of a dipolar spherical NP. In this particular case, it is defined as,

$$Fa = 9 \left| \frac{\epsilon}{\epsilon + 2\epsilon_s} \right|$$

where  $\epsilon$  is the dielectric function of the metal and  $\epsilon_s$  is the dielectric function of the surrounding medium. Figure 2 shows the value of the maximum value of Fa for different metals including alkaline earth metals (s-metals), transition metals (d-metals), and post-transition metals (sp-metals). From group 2, magnesium (Mg) has been selected as representative of the s-metals. We also have considered most of the transition metals: group 4 titanium (Ti); group 6 chromium (Cr), molybdenum (Mo), and tungsten (W); group 7 rhenium (Re); group 8 iron (Fe) and ruthenium (Ru); group 9 cobalt (Co) and rhodium (Rh); group 10 nickel (Ni), palladium (Pd), and platinum (Pt); and group 11 copper (Cu), silver (Ag), and gold (Au). Finally, as sp-metals, we analyze group 13 metals, aluminum (Al), gallium (Ga), and indium (In).



**Figure 2.** Faraday number  $Fa$  of the selected metals.

In general, transition metals (d-metals) present  $F_a$  numbers between 10 and 20, with Mo, Rh, Ru, Cu, and Au having the largest values. The plasmonic behavior of transition metals is consistent with their strong interband absorption upon visible or UV illumination, which is responsible for their high optical losses. This points out the fact that Au has not the most efficient plasmonic response when compared to other metals. Nevertheless, it is a very extended metal in plasmonics because of its oxide-free nature and low reactivity, which in turn, and as we will see further on, are characteristics that are not applicable for the application explored here.

The transition metal with better plasmonic performance is Ag, whose is  $F_a = 467$ . In this case, the plasmonic resonances are generally very intense and sharp with excitation wavelength above the interband transitions. When considering the stability of Ag nanostructures, it is well known the problem of their oxidation when exposed to ambient conditions. Another problem to consider is the tarnishing of Ag nanostructures when exposed to sulfur rich environments<sup>16,17</sup> and/or interfaced with sulfur-rich compounds. Therefore, coupling Ag with some of the chalcogenides materials developed in this project such as GaS,  $Sb_2Se_3$  or GeS can be problematic in terms of the stability of the nanoantennas. Proof of this will be given in section 8.

The material with the highest  $F_a$  number is s- metal Mg. However, Mg is completely ruled out because of its poor environmental stability. Recent experiments exploring the possibility of Mg-based plasmonics were performed by deposition 25 nm radius hemispherical-shape Mg structures on sapphire. Although the spectra obtained after deposition in UHV showed a strong LSPR, after only one week of air exposure, the LSPR of the same NPs was completely quenched.<sup>18</sup> Basically, the native oxide MgO forms aggressively upon exposure to air as oxygen rapidly diffuses through the porous oxide into the metal.

Finally, we have considered *sp*-metals, in particular Al, Ga and In, which they present decreasing values of  $F_a$ . Nevertheless, this values are higher than those of most transition metals and comparable to that of Ag. Once again, it is known that Al and In nanoantennas have ambient stability issues. Indium was found to form a similarly aggressive consumptive oxide such as Mg.<sup>18</sup> Both Ga and Al form self-terminating oxide layers, which in the case of Al is thicker than for the case of Ga (5 nm vs 1 nm). Aluminum is a good plasmonic metal and has already been used successfully for a number of CMOS-compatible plasmonic applications. However, the melting temperature of Al, at 660 °C, is very close to that of most commonly used PCMs (e.g., conventional  $Ge_2Sb_2Te_5$  melts at 630 °C,  $Ge_1Sb_2Te_4$  at 614 °C); thus, there is a danger that during the PCM amorphization process any thermally adjacent Al plasmonic layer might also melt, leading to device degradation. Gallium nanoantennas, on the other hand, have been demonstrated by us to be stable up to temperature as high as 600°C.<sup>19</sup>

It is clear that any of the above plasmonic metal options should ideally be CMOS-compatible, to allow for, ultimately, easy integration into PIC fabrication lines, and Gallium is also CMOS-compatible.

Therefore, considering all the arguments above, from now on we will focus on Ga as plasmonic material.

### 3.2 Gallium as an alternative plasmonic metals to be coupled to chalcogenides PCMs

Gallium (Ga) is most commonly known as a liquid metal with a melting temperature just above room temperature (29.7 °C). Ga is nontoxic, biocompatible, environmentally stable, flexible, stretchable and deformable with low viscosity, and possesses excellent thermal and electrical conductivities, as well as high reflectivity. Liquid Ga NPs have been proposed in plasmonics due to their LSPRs tunable from the UV to the NIR spectrum, and their self-passivating ultra-thin oxide shell (~1 nm) that enables the NPs high stability.

Polymorphism is another attractive feature of Ga which has been recently analysed.<sup>11</sup>

So far, up to five different Ga crystalline structures have been reported with a different percentage of metallic and covalent Ga bonds that translates into different electronics structures and, consequently, into different optical properties. At low pressure and temperatures  $T > 27$  °C, Ga is liquid, while below this temperature, it solidifies in the  $\alpha$ -Ga orthorhombic crystal structure that belongs to the Cmce (no. 64) space group with eight atoms in the unit cell. Additional metastable Ga phases have been reported with decreasing temperature, i.e.,  $\beta$ -Ga with a melting temperature ( $T_m$ ) of 256.8 K, space group symmetry C2/c (no. 15) and eight atoms in the unit;  $\gamma$ -Ga ( $T_m = 237.6$  K) with a complex Cmcm (no. 63) structure and 40 atoms/unit cell;  $\epsilon$ -Ga ( $T_m = 244.6$  K) whose crystalline structure is still unknown; and  $\delta$ -Ga ( $T_m = 253.8$  K), which crystallizes in a rhombohedral structure with space group symmetry R3m (no. 166) and a unit cell with 22 atoms. Moreover, by increasing pressure, this polymorphism includes also Ga(II) and Ga(III). Indeed, recently, all those phases have been demonstrated to occur depending on, for instance, the cycles of cooling and heating of the Ga thin film, on deposition methodology of Ga nanoparticles and on their size, as well as on the epitaxial relationship with the substrate where Ga thin films or nanoparticles are deposited on.<sup>20</sup>

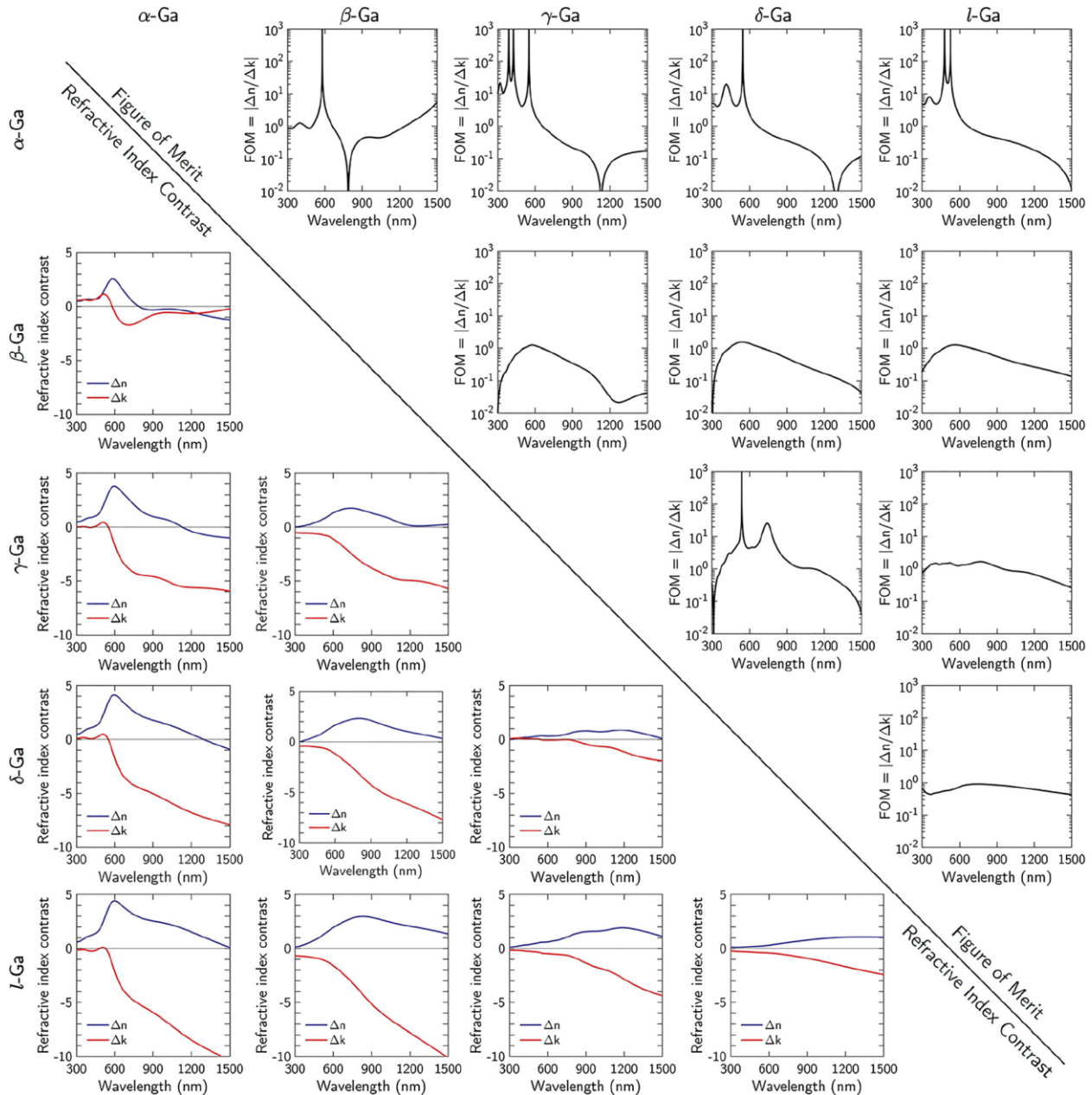
In terms of their optical properties,  $\alpha$ -Ga has strong interband transitions at 1050 and 570 nm, which are smoothed in  $\beta$ -Ga at approximately 660 nm, while  $\gamma$ -Ga and  $\delta$ -Ga display a dispersion profile typical of an ideal Drude metal. Finally, l-Ga presents a perfect Drude-like behavior. Therefore, the following trends of metallic character can be established:

$$l\text{-Ga} > \delta\text{-Ga} > \gamma\text{-Ga} > \beta\text{-Ga} > \alpha\text{-Ga}$$

Given the differences in dielectric function between the different Ga phases, Ga itself has been explored as phase-change material. Figure 3 plots the refractive index contrast ( $\Delta n$  and  $\Delta k$ ) calculated for different pairs of Ga phases in the lower diagonal. As pointed out by Abdollahramezani et al.,<sup>21</sup> the key condition for optimal

optical modulation or switching consists in achieving large changes in the optical constants within the operational spectral region of the device. Ideally, this large change in the optical constants should entail a high contrast in the real part of the refractive index ( $\Delta n$ ) with small induced optical losses ( $\Delta k \approx 0$ ).<sup>21</sup> Therefore, the in FOM  $\Delta n/\Delta k$  defined as the ratio of the index change to the loss change serves to compare PCMs. In bulk materials,  $\Delta n$  and  $\Delta k$  cannot be independently controlled because the real and imaginary parts of the complex refractive index are Kramers-Kronig related. Consequently, a change in the real part of the refractive index will lead to a change in the imaginary part (and vice versa) in a way that the Kramers-Kronig relation remains preserved. In light of this, in the lower diagonal of Figure 3 it is plotted the FOM for each pair of Ga phases.

The phase transitions involving  $\alpha$ -Ga show the highest FOM in the UV-visible range (300–800 nm). Specifically, the  $\alpha$ - to  $\beta$ -phase transition shows a pronounced FOM peak, i.e.,  $\text{FOM} > 10^3$ , at 580 nm. Interestingly, the  $\alpha$ - to  $\gamma$ -phase transition shows several peaks in the FOM, i.e., three pronounced peaks at 386, 428, and 549 nm and an intermediate intensity (i.e.,  $\text{FOM} = 22$ ) at 318 nm. The FOM for the  $\alpha$ - to  $\delta$ -phase transition shows a pronounced peak at 548 nm and an intermediate peak at 410 nm. Finally, the  $\alpha$ - to  $\iota$ -phase transition shows two pronounced peaks at 480 and 526 nm and an intermediate (i.e.,  $\text{FOM} \sim 10$ ) peak at 360 nm. Another interesting transition involving high values of the FOM is the  $\gamma$ - to  $\delta$ -phase transition, with a pronounced and an intermediate peak at 540 and 743 nm, respectively. All other transitions have poor values of  $\text{FOM} \leq 1$ .

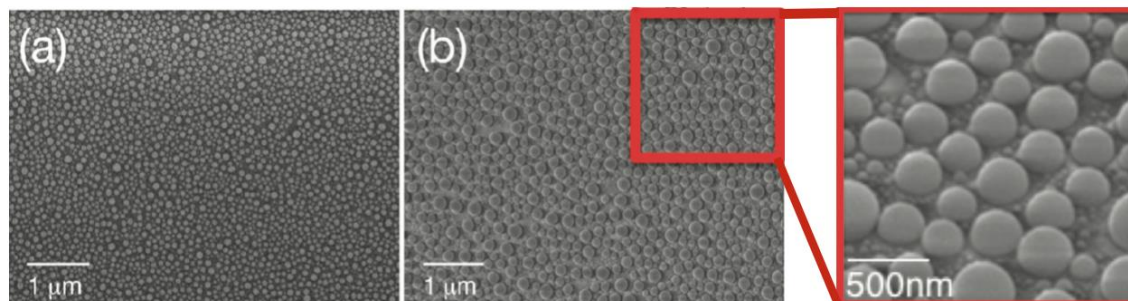


**Figure 3.** Figure-of-merit (FOM) and refractive index contrast in Ga phase transformation. Combination matrix plot of the FOM  $\Delta n/\Delta k$  (upper diagonal matrix) and refractive index contrast  $\Delta n$  and  $\Delta k$  (down diagonal matrix) on phase transition between Ga phase pairs.

Although Ga shows potential as PCM, its main drawback is that switching between phases requires ultracool environments and cooling cycles. From the practical point, cooling processes are more technologically demanding than the typical heating process required to crystallize and amorphize the prototypical chalcogenides PCMs that will be considered in PHEMTRONICS. Therefore, for the work presented in this deliverable, only liquid Ga NPs are studied.



Gallium NPs are generally fabricated by evaporating Ga and its condensation on a substrate forming hemispherical NPs consisting of *l*-Ga and stabilized by the ultrathin oxide layer. This morphology can be appreciated in the scanning electron microscopy images in Figure 4.



**Figure 4.** Scanning electron microscope images of different samples of Ga NPs. The Ga NPs take an hemispherical shape when deposited on a substrate.

Interestingly, the dielectric function of *l*-Ga presents a perfect Drude-like behavior as shown in Figure 5a. In the Drude model, metal electrons are considered as molecules of a classic gas. Interestingly, no interband transition characterizes the Ga dielectric function in the visible range; this would potentially reduce losses.

When a metal nanoparticle as *l*-Ga is illuminated, the free charge tends to oscillate with the same frequency as that of the incident beam. This phenomenon leads to Localized Surface Plasmon Resonances (LSPR). As a consequence, the incident field is both confined in the nanoparticle and intensified in its surroundings leading to the possibility of establishing very strong light-matter interactions. These regions of intensification are known as *hot-spots* and can be analyzed through Mie theory if the nanoparticle size is above 5-10 nm.<sup>22</sup> Mie theory describes the scattering of an electromagnetic plane wave by a homogeneous sphere.<sup>23</sup> The solution takes the form of an infinite series of spherical multipole partial waves. Each multipole corresponds to a different resonance-order (dipole –  $a_1$ , quadrupole –  $a_2$ , ...).

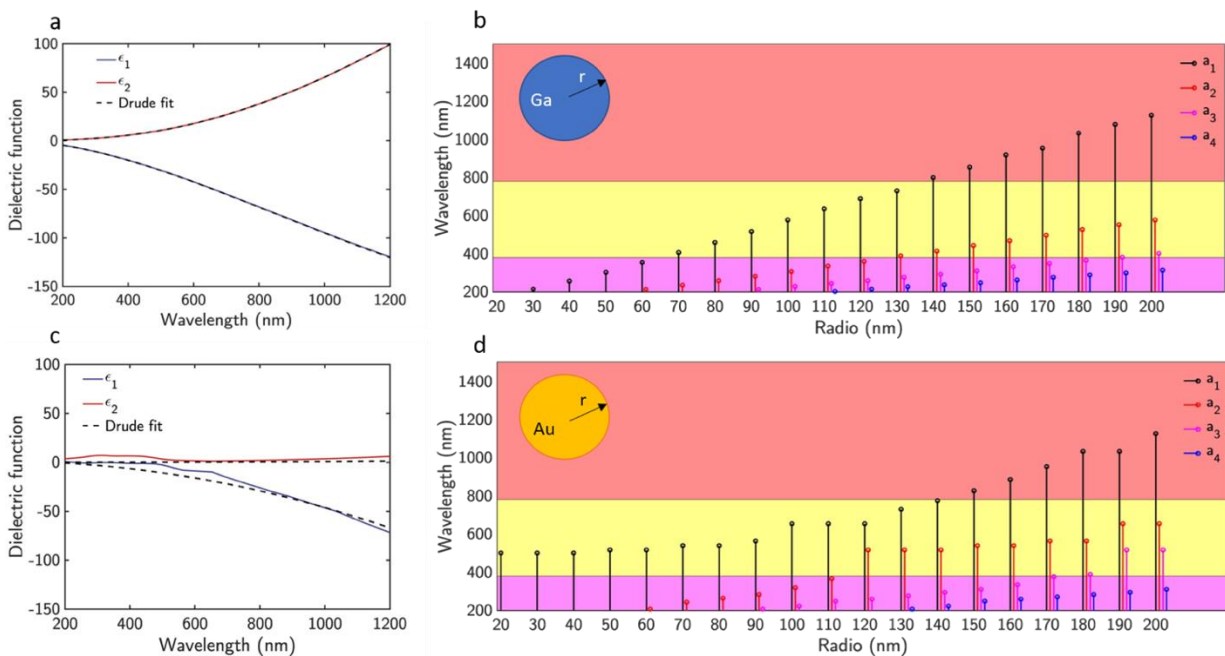
The enhancement of the electric field generated by the LSPR resonances excited in Ga NPs are expected to be exploited as a route to help in the switching process between the amorphous and the crystalline phases of the PCM. In the absence of nanoantennas, the laser induced phase-change is a consequence of light absorption in the PCM that is translated in local heating. Therefore, as pointed out by Delaney et al.,<sup>24</sup> the reversible switching requires a critical amount of absorption in the materials to achieve the required temperature states. Introducing nanoantennas in our systems will enable a better and more controlled coupling of light into the PCM material leading to a more effective light absorption process by the PCM. Moreover, given the localized electric-field enhancement produced at the NPs (hot spots), lower laser powers are expected to be required to switch the phase of the PCM when compared to the system with no plasmonic coupling.



From Figure 5b it can be inferred that the Ga nanoantenna radius can be used as parameter to tune the LSPR to the wavelengths of interest in PHEMTRONICS. This plot proof that the range in which Ga LSPRs can be tuned ranges 200 nm to 1600 nm. This include wavelengths for which the plasmonic antennas act as plasmonic actuators to trigger the crystallization/amorphization of the PCM (i.e., wavelengths above the energy bandgap of the PCM), or those in which some active and reconfigurable plasmonic devices (e.g. photodetectors or switches) proposed in PHEMTRONICS are expected to operate (i.e. telecom 1550 nm and visible 550 nm).

For comparison, the dielectric function and spectral position of the localized surface plasmon resonant modes in Au nanospheres as function of their size are plotted in Figures 5c,d. The dielectric function of Au present interband transition below  $\sim 500$  nm inhibiting the excitation of LSPRs below that threshold. For this reason, gold dielectric function cannot be fitted with Drude model for short wavelengths. Moreover, for the smallest sizes ( $R = 20$  to  $50$  nm) the LSPR wavelength shows no tunability since it stays fixed at 500 nm. It is important to consider that, for the applications interested here, the Au NPs have to be supported in a substrate. It is known that the effect of the substrate on the of NPs LSPR is a red-shift.<sup>25</sup> Thus, it is expected that for this materials only wavelengths above 550-600 nm are accessible, inhibiting the coupling of gold with the energy band gap of some of the low-loss PCMs at optical frequency that will be considered in PHEMTRONICS.

Therefore, the limited tunability into lower wavelengths in the case of Au is a clear disadvantage when compared to Ga.



**Figure 5.-** Dielectric function of (a) liquid gallium and (b) gold. Blue and red lines represent the real and the imaginary part of respectively. Dashed lines correspond to theoretical Drude model fit. Dipolar ( $a_1$ ), quadrupolar ( $a_2$ ), octopolar ( $a_3$ ) and hexadecapolar ( $a_4$ ) resonances as a function of the wavelength and the size of (b) Ga and (d) Au NPs. Red, yellow and violet colors represent NIR, VIS and UV respectively.

As an example, we consider PHEMTRONICS PCM gallium sulfide (GaS). From high accuracy spectroscopic ellipsometry measurements, the band gap of the crystalline of this material has been established to be 2.35 eV (530 nm) and blue shifts for two-dimensional (2D) GaS reaching values of 3.1 eV for monolayer GaS. In the case of Ga NPs, tuning the LSPR to be resonant with the bandgap of the PCM can be easily achieved by selecting the adequate size of the NP. However, as explained above, for Au nanoparticles, coupling light efficiently into 2D GaS would not be possible due to the difficulty of matching the LSPR of Au NPs in a realistic configuration with the bandgap of GaS. Therefore, it can be concluded that, due to the wide tunability of the LSPRs excited in Ga NPs, it can be considered a plasmonic material that can be coupled to any PCMs with band gaps as high as that of GaS (2.35 eV) to those with gaps as low as GST (0.5 eV).

In light of this, in this deliverable, nanoantennas made of *I*-Ga are going to be considered as plasmonic units. In particular, we will focus on the plasmonic actuation to activate the crystallization/amorphization of the PCM.

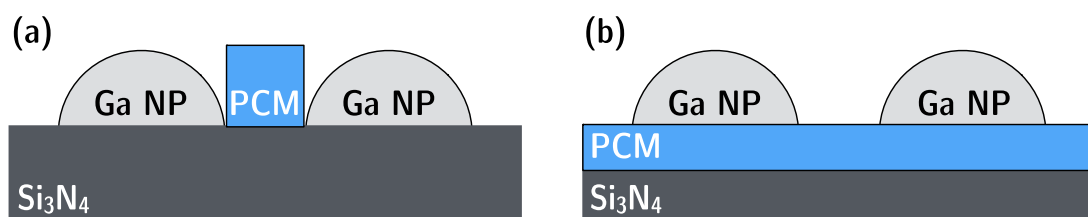
### 3.3. Ga dimer nanoantennas as plasmonic actuators

We will consider two Ga hemispheres in close proximity, i.e., a dimer, in order to explore and quantify possible cooperative effects between the individual nanoantennas.

The dimers will be used in two configurations:

- on top on a  $\text{Si}_3\text{N}_4$  substrate with the PCM located in the dimer's gap (Figure 6a). Here, the PCM acts as a direct switching device since its transmission changes when phase changes.
- on top of a PCM thin layer located on a  $\text{Si}_3\text{N}_4$  waveguide (Figure 6b). Here the PCM acts a switching coupler to the waveguide because the PCM interacts through its evanescent field with the waveguide underneath.

These two configurations have already been adopted in previous works by the PHEMTRONICS partner WWU<sup>8,26</sup> using conventional gold plasmonic nanoantenna. Here, we implement the concept using Ga nanoantennas. The first configuration is equivalent to that reported by WWU in ref. 8 and the second configuration is similar to that proposed in ref. 26. Therefore, we start from this expertise and indication of geometry to evaluate Ga dimer nanoantennas.



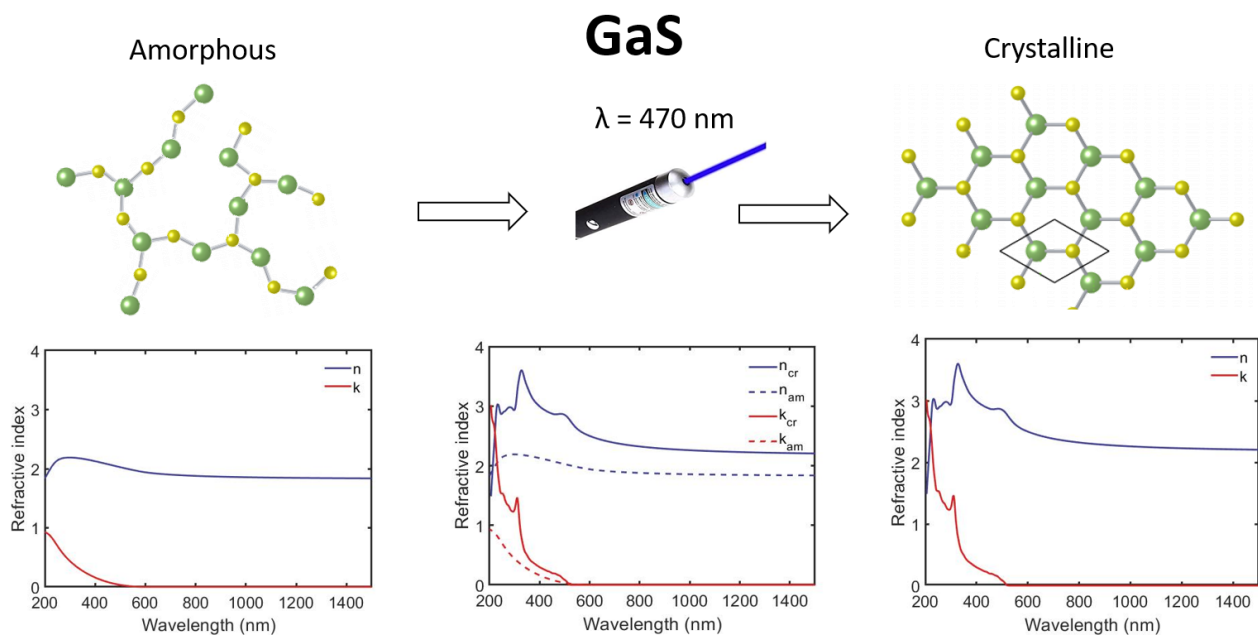
**Figure 6.** (a) Ga hemisphere dimer on top on a  $\text{Si}_3\text{N}_4$  substrate with the PCM located in the dimer gap; (b) Ga hemisphere dimer on top of a PCM layer located on a  $\text{Si}_3\text{N}_4$  waveguide.

In order to couple light into the wide bandgap PCMs, the radius of the hemispheres has to be tuned to have the LSPR of the Ga dimer resonant with the wavelength of interest. In our case, the wavelength should be above the energy bandgap of the PCM to ensure light absorption.

In this deliverable, the PCM used as an example investigated is gallium sulfide (GaS) which has an energy bandgap 2.40 eV (530 nm), and has been selected by the consortium as one of the PCMs to be further optimized.

By experiments performed at partner CNR NANOTEC, the transition from amorphous to crystalline GaS and viceversa has been obtained with laser wavelengths of 532 nm and of 470 nm. Therefore, to maximize the coupling of this light into GaS the Ga dimer nanoantenna LSPR has to be designed to match and be resonant with those wavelengths. Here, we report the calculations for the specific case of 470nm, whereas for 532 similar approach and calculations have also been run. Indeed, it is worth noting that similar behavior can be achieved for any wavelength above the energy band gap of GaS, which would require a small tuning on the nanoantenna parameters, i.e., the hemisphere radius.

The refractive index of both amorphous and crystalline GaS phases are plotted in Figure 7.

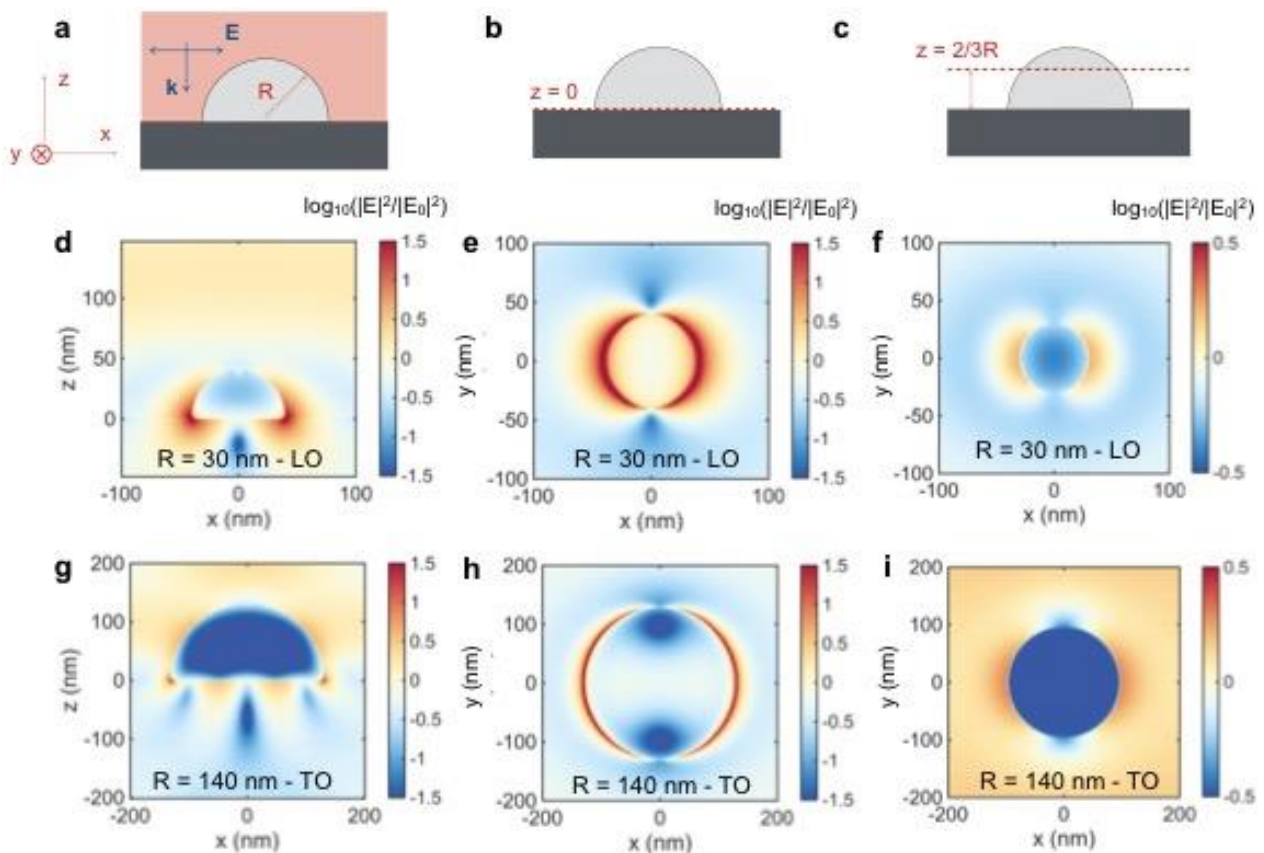


**Figure 7.** Amorphous and crystalline phases of gallium sulfide. The transition between both can be governed illuminating with a laser of wavelength of 470 nm.

The resonant wavelength of the nanoantennas system selected here, i.e., Ga hemispheres dimer, cannot be directly obtained from Mie theory because there is no analytical solution. Consequently, the simulation of the Ga hemispheres dimer was made using finite-difference time-domain (FDTD) simulations (LUMERICAL), which is a numerical analysis technique used for modelling computational electrodynamics (finding approximate solutions to the associated system of differential equations by discretization). The light source for the calculations has been chosen to a plane wave linearly polarized with the electric field parallel axis of

the dimer. This polarization has been chosen to enhance the interaction between the hemispheres composing the dimer.<sup>27</sup>

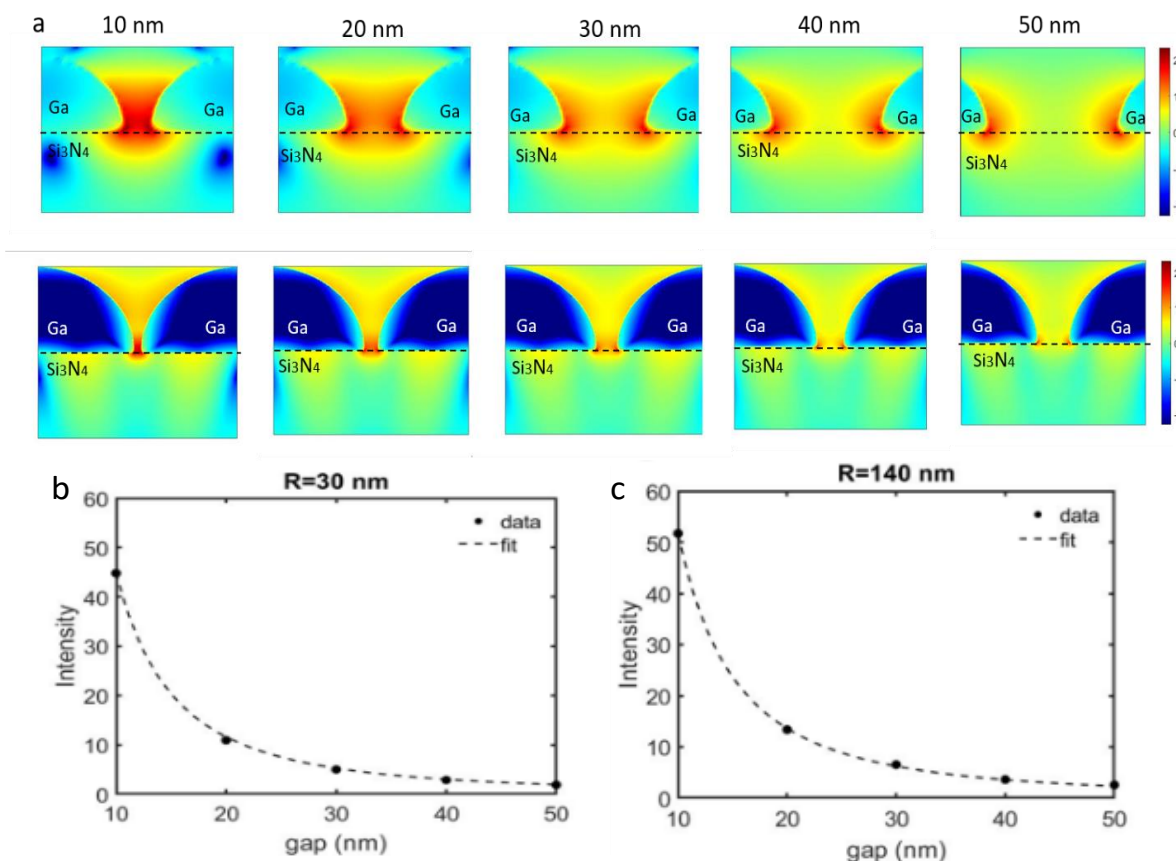
FDTD simulations have pointed out that there are two radii that generate a maximum near-field enhancement in the gap of dimer by either coupling the LO and TO modes that characterize Ga hemispheres: a radius of 30 nm results in longitudinal modes (LO) resonant at 470 nm, whereas for a radius of 140 nm the transverse modes (TO) resonates at 470 nm. In order to have a better understanding of these two resonant modes characteristic of Ga hemispherical nanoparticles, Fig. 8 shows the near-field enhancement maps in different planes for the LO and TO-LSPRs. Figure 8 shows the near-field ( $|E|^2$ ) spatial distribution for the LO and TO modes, which are quite different. These maps are plotted in a plane perpendicular to the substrate that contains the propagation direction ( $\mathbf{k}$ ) and electric field polarization vector ( $\mathbf{E}_0$ ) of the incident beam (Fig. 8a, side view) and in two planes at different heights parallel to the substrate, i.e., at the substrate surface (Fig. 8b,  $z=0$ , top view), and at  $z=(2/3)R$  (Fig. 8c, top view). Noteworthy, near-field enhancement maps are plotted in logarithmic scale. Specifically, the LO-mode hot-spots are localized at the Ga hemisphere – substrate interface. The LO resonance is purely dipolar, and the electron plasma oscillates with the largest amplitude along the hemisphere diameter, parallel to the interface Ga hemisphere – substrate interface.



**Figure 8.** Near-field enhancement maps plotted (a) in the plane containing the incident beam wave vector ( $\mathbf{k}$ ) and polarization ( $\mathbf{E}_0$ ), and in planes parallel to the substrate (b) at  $z=0$  (interface with the substrate) and (c) at  $z=(2/3)R$ . Those maps are shown for the (d-f) LO-LSPR of Ga NPs with  $R = 30$  nm, and for the (g-i) TO-LSPR of Ga NPs with  $R = 130$  nm on a  $\text{Si}_3\text{N}_4$  substrate.

The TO-mode hot-spots are distributed over the surface of the Ga hemisphere (e.g. compare  $|E|^2$  maps in Fig. 8c for  $z = (2/3)R$ ). The TO mode can be associated to a higher order resonant mode. This different spatial distribution is relevant to rationalize the coupling strategies of the near-field enhancement produced by the nanoantennas into the PCMs inclusions and layers.

Moving to the dimer configuration, the gap between the hemispherical nanoparticles is a critical parameter to take into account during the analysis of the near-field enhancement generated by the dimer. The near-field enhancement at the center of the gap becomes higher with decreasing gap lengths. The near-field enhancement maps in logarithmic scale are shown in Fig. 9a for: (i) an incident wavelength of  $\lambda=470$  nm, (ii) different gaps (from 10 to 50 nm) and (iii) for nanoantennas' radii of 30 nm – LO mode (first row) and 140 nm – TO mode (second row). The near-field enhancement distribution around the dimer generated by the nanoantennas of radius 30 nm consists on two interacting lobes at the substrate-NP interface compatible with a dipolar resonance (LO modes). For the size of 140 nm, additional interacting lobes appear in the near-field enhancement distribution compatible with a higher order resonance (TO modes). The value of the enhancement in the middle of the nanoantenna gap is shown in Figs 9b and 9c for radius of 30 nm and 140.



**Figure 9.-** (a) Enhancement of the scattered field in logarithmic scale when the incident wavelength is  $\lambda=470$  nm, for different gaps (10 -50 nm) , and for the radio 30 nm (first row) and 140 nm (second row). (b) and (c) Enhancement in the middle of the nanoantennas for different gaps and for the radius 30 nm and 140 nm respectively.

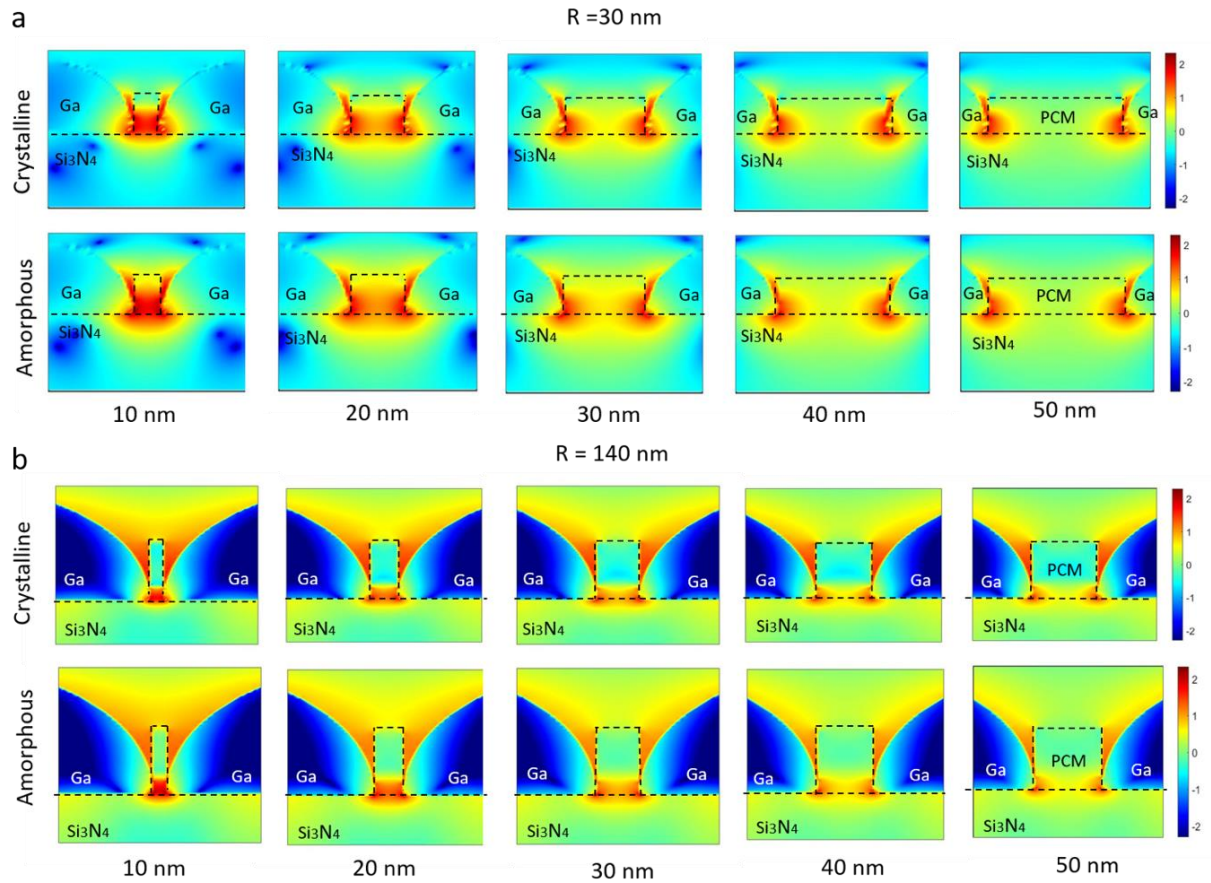


When the value of the gap increases, the enhancement decreases. In both cases, the relation between both magnitudes can be fitted to the equation  $E = a/g^b$ , where  $E$  is the enhancement,  $g$  is the gap (in nm) and  $a$  and  $b$  are the modelling parameters. For the  $R = 30$  nm – LO mode dimer the parameters are:  $a = 4057$  and  $b = 1.955$ . For the 140 nm – TO mode dimer the parameters are:  $a = 4373$  and  $b = 1.927$ . Once the electromagnetic behavior of the bare dimer is studied, we turn into the study of the proposed dimer configurations incorporating the PCM as presented in Figure 6.

First, we will focus on the configuration in which the PCM is placed at the gap of Ga hemispheres dimer. For a wavelength of 470 nm, the refractive index of the amorphous and crystalline phases of GaS are  $2.05 + 0.05i$  and  $2.85 + 0.25i$  respectively. The crystalline phase, at this wavelength, presents a higher absorption coefficient, which implies a more efficient absorption of the electromagnetic fields, but also higher optical losses. The width of the PCM is equal to the gap of the Ga nanoantennas, while the thickness of the PCM is half of the nanoantenna radius (in the present case thicknesses of 15 and 70 nm for  $R = 30$  and 140 nm dimers). Thus, the larger the nanoantenna gap, the largest the thickness of PCM that needs to be deposited between the hemispherical nanoantenna.

The near-field enhancement, in logarithmic scale, is shown in Fig 10a and 10b for: (i) an incident wavelength of 470 nm, (ii) different gaps ranging from 10 to 50 nm, (iii) amorphous (bottom row) and crystalline (top row) GaS phases, and (iii) nanoantennas sizes of 30 nm – LO mode (Fig 10a) and 140 nm – TO mode (Fig 10b). When considering the electromagnetic field inside the PCM, higher values can be achieved for the amorphous phase given its lower extinction coefficient when compared to the crystalline phase. For both nanoantenna radii considered here (10a and 10b), the electric field penetrates inside the PCM in the regions where the material is in contact with the Ga nanoantennas. This is due to the boundary conditions of the electric field at the Ga-GaS interface and to the refractive index contrast between air and GaS.

**Taking into account these considerations, by maximizing the contact area between the GaS and the Ga nanoantenna, it is possible to maximize the penetration into the PCM of the hot spots generated by the dimer and thus, maximize light absorption in the PCM.**

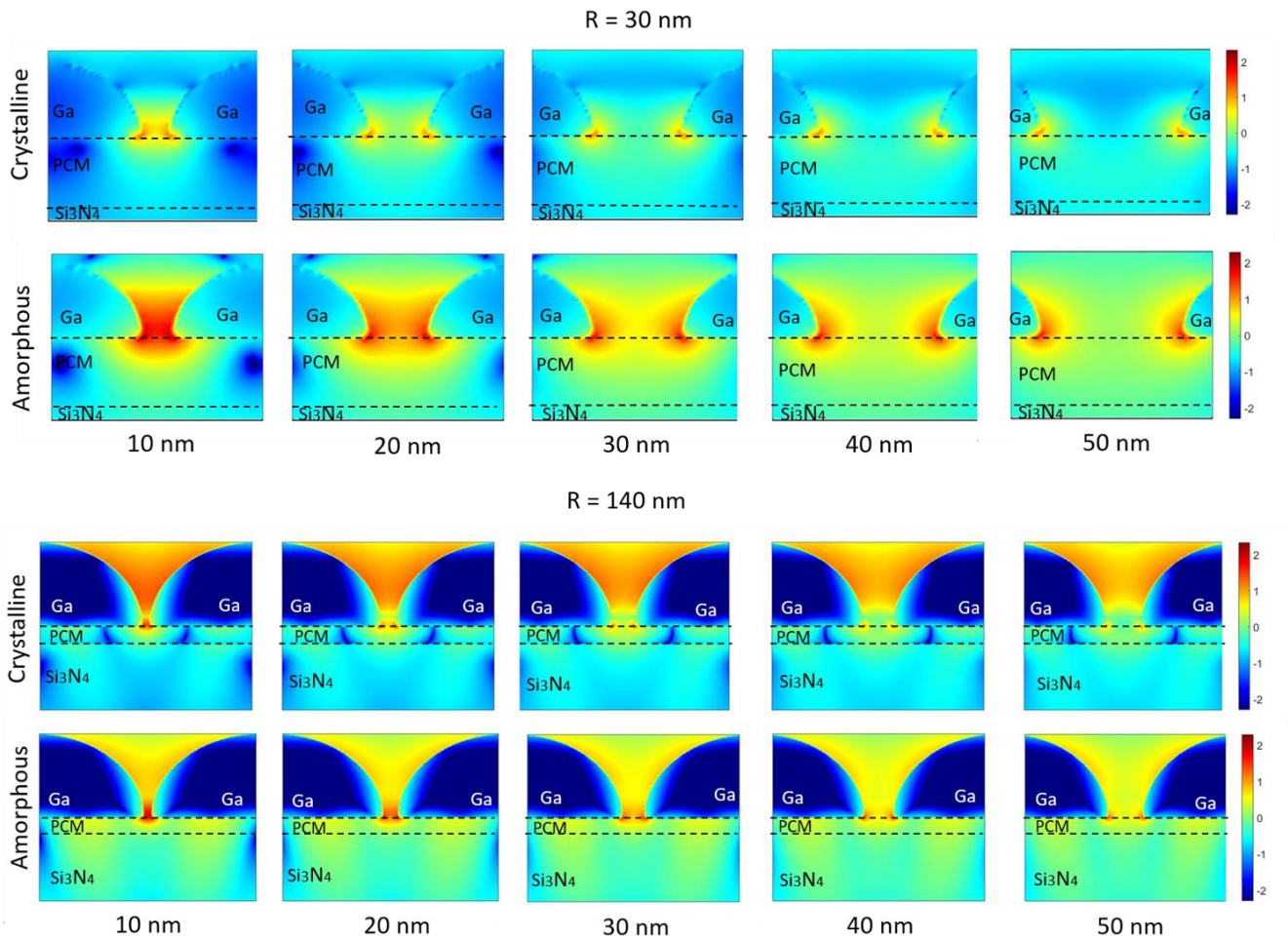


**Figure 10.-** (a) Enhancement of the scattered field in logarithmic scale when the incident wavelength is  $\lambda=470$  nm, for different gaps (10 -50 nm) , for crystalline (1<sup>st</sup> row) and amorphous (2<sup>nd</sup> row) and for a radius of the nanoantennas of 30 nm. (b) Enhancement of the scattered field in logarithmic scale when the incident wavelength is  $\lambda=470$  nm, for different gaps (10 -50 nm) , for crystalline (1<sup>st</sup> row) and amorphous (2<sup>nd</sup> row) and for a radius of the nanoantennas of 140 nm. The thickness of the PCM is 15 nm for a) and 70 nm for b).

Another studied configuration consists in the deposition of Ga nanoantennas on top a thin layer of PCM. For this study, the thickness of the GaS layer has been set to 30 nm. The near-field enhancement in logarithmic scale is shown in Fig 11a and 11b for: (i) incident wavelength is 470 nm, (ii) different gaps ranging from 10 to 50 nm, (iii) both amorphous (bottom row) and crystalline (top row) phases in the GaS layer, and (iv) nanoantennas sizes of 30 nm – LO mode (Fig 11a) and 140 nm – TO mode (Fig 11b).

For both radii of 30 nm and 140 nm respectively in Fig. 11a and 11b, large differences in the electromagnetic behavior between amorphous and crystalline phases can be seen. This is because the real part of the refractive index of the crystalline phase ( $n=2.85$ ) is larger than that of Si<sub>3</sub>N<sub>4</sub> ( $n=2.04 + 0i$ ), leading to a redshift of the resonant wavelength. On the contrary, the GaS amorphous phase shows a value of the refractive index ( $n=2.05 + 0.05i$ ) similar to that of Si<sub>3</sub>N<sub>4</sub> at the considered wavelength of 470 nm, generating a clear index matching between the two materials. In fact, the maps in the second row of Fig 11b are similar to the maps

reported in the second row of 9a, (as no PCM between the Nanoantenna and the  $\text{Si}_3\text{N}_4$  due to the index matching between GaS and  $\text{Si}_3\text{N}_4$ ).



**Figure 11.-** (a) Enhancement of the scattered field in logarithmic scale when the incident wavelength is  $\lambda=470$  nm, for different gaps (10 -50 nm), for crystalline (1<sup>st</sup> row) and amorphous (2<sup>nd</sup> row) and for a radius of the nanoantenna of 30 nm. (b) Enhancement of the scattered field in logarithmic scale when the incident wavelength is  $\lambda=470$  nm, for different gaps (10 -50 nm) , for crystalline (1<sup>st</sup> row) and amorphous (2<sup>nd</sup> row) and for a radius of the nanoantenns of 140 nm. In a) and b) the PCM is situated under the nanoantenna and its thickness is of 30 nm.

The near-field enhancement inside the PCM has been averaged for both the studied configurations (PCM GaS placement) considering the R = 30 and 140 nm nanoantennas radii. The configuration and mode (either LO – 30 nm or TO – 140 nm) which generate the highest near-field enhancement inside PCM GaS depending on its phase can be inferred from Figure 12. The geometrical parameters of the PCM in each case are shown in the inset. Although this size is different for each configuration and mode (LO and TO), they are normalized to the radius R of the Ga NPs. In the first configuration, the thickness of the PCM is R/2, i.e, 15 nm for the R = 30 nm – LO mode nanoantennas and 70 nm for the R = 140 nm – TO mode nanoantennas. The width of the PCM is equal to the nanoantenna gap. Conversely, in the second configuration, the thickness of the PCM is



fixed to 30 nm and the width of the averaging zone varies for each mode, being equal to twice the radius (the dimer nanoantenna) plus the gap (see yellow shadowed region in Fig. 12). Specifically, for  $R = 30$  nm – LO mode nanoantennas, the width is 70 nm ( $30 + 10 + 30$ ) and for  $R = 140$  nm – TO mode nanoantennas the width is 290 nm ( $140 + 10 + 140$ ).

**The highest near-field enhancement averaged over the PCM volume is generated for the 30 nm – LO mode nanoantennas in the first configuration, i.e., with PCM placed at the gap of the dimer (Fig 12a).**

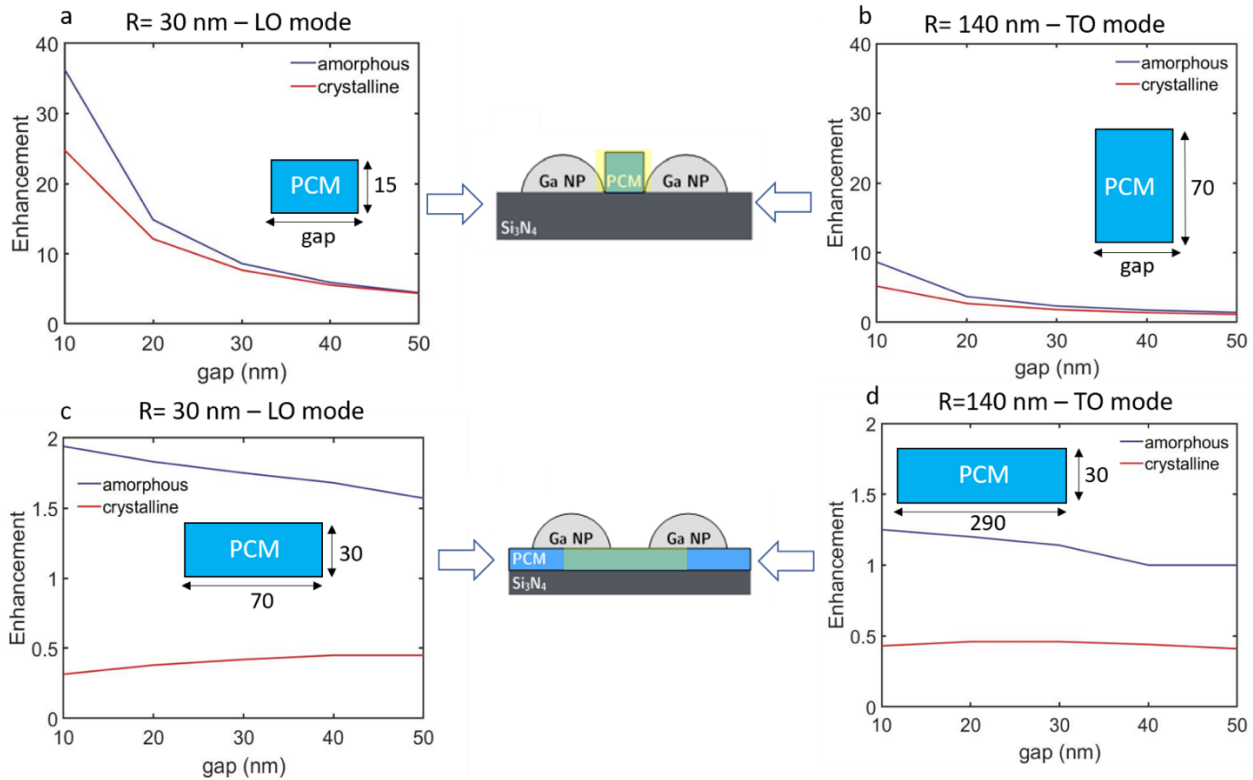
The LO mode presents hot spots confined at the substrate-nanoantenna interface, matching the region of contact area between the PCM and the Ga nanoantennas. The values are particularly high for the smallest gap. This is because the inclusion of a small volume of PCM in a small gap enables a strong coupling between hot spots generated in interacting hemispheres of the dimer while maintaining a high contact area with the Ga hemisphere (see Figure 10a). Conversely, in this configurations, low values of the near-field enhancement averaged over the PCM volume are achieved for the  $R = 140$  nm – TO mode. For this mode, the hot spots are no longer confined at the interface between the nanoantennas and the substrate. The hotpost distribution is located at the upper part of the gap where there is no contact area between PCM and Ga hemispheres, making the coupling of the near-field into the PCM more challenging.

**The lowest averaged enhancement is obtained with the second configuration, i.e., Ga dimer onto the PCM layer deposited on  $\text{Si}_3\text{N}_4$ .**

The hotspot is mainly concentrated in the gap and decreases as the PCM layer thickness increases. The deposition of the PCM under the Ga dimer shifts the resonant wavelength of Ga dimer, as the interaction between Ga NPs in the dimer is strictly dependent on the electromagnetic behavior of the material on which they are deposited (namely its refractive index). GaS present higher refractive index than  $\text{Si}_3\text{N}_4$ , and hence, the resonant wavelength of the LSPR shifts to higher wavelengths, decreasing the enhancement at the wavelength of interest (470 nm).

Here we point out that, for the study of plasmonic units, we have reported as an example the PCM of GaS because within WP2 the dielectric function of both crystalline and amorphous phases have been established with high accuracy.

The calculations presented here for Ga nanoantennas coupled to GaS will be extended to other PHEMTRONICS PCMs such as  $\text{Sb}_2\text{S}_3$  and GeS. Only small tuning on the Ga NPs parameters will be needed to optimize the system to other PCMs.



**Figure 12.-** Average enhancement generated inside the PCM in the first configuration (PCM in the gap) and for LO (a) and TO (b) modes respectively. Average enhancement generated inside the PCM in the second configuration (PCM in the upper part of the silicon nitride waveguide) for LO (c) and TO (d) modes respectively. Blue line represents the amorphous state and red line is for crystalline PCM. With a yellow rectangle are indicated the regions in which the near-field enhancement average has been performed.

## 4. Photothermal Plasmonics

Metal nanoparticles can help to control the temperature at the nanoscale. When excited with light at the plasmon resonance wavelength, nanoparticles can increase the amount of light absorbed and convert it into heat, becoming a nano-heat source. When the NP is coupled to a PCM material, this heat can be transfer into it to activate and/or contribute to its crystallization/amorphization process.

The heat-generation process involves not only absorption of incident photons, but also the heat transfer from the nanoparticle to the surrounding medium. This happens as follows: the incident electric field strongly drives mobile carriers of the metal, heating the material owing to the energy gained by these carriers (Joule effect). Then, heat diffuses from the nanostructure heating up the surrounding medium. If phase transformations are not considered, the distribution of temperature around nanoparticles can be described solving the usual heat transfer equation.

$$\rho(\mathbf{r})c(\mathbf{r})\frac{\partial T(\mathbf{r},t)}{\partial t} = \nabla k(\mathbf{r})\nabla T(\mathbf{r},t) + Q(\mathbf{r},t) \quad (1)$$

where  $\mathbf{r}$  and  $t$  are the position and time,  $T(\mathbf{r},t)$  is the local temperature and the material parameters  $\rho(\mathbf{r})$ ,  $c(\mathbf{r})$  and  $k(\mathbf{r})$  are the mass density, specific heat and thermal conductivity, respectively. The function  $Q(\mathbf{r},t)$  describes the energy source which is directly related to the amount of light dissipated (resistive losses). The solution of Eq. (4) has a transient state, and after a characteristic time, it reaches its steady state. Thermal processes in metals are fast (ns), which means that a steady state is rapidly reached for typical incident powers and metal nanoparticle dimensions.

Maxwell equations with appropriate boundary conditions must be solved to obtain the resistive losses being necessary to rely on numerical methods for most of the geometrical topologies. In our case, the entire light absorption process and its subsequent heat transfer to the surrounding medium was modelled by means of a finite element method (COMSOL Multiphysics) and assuming that the particles were illuminated with linearly polarized light.

The electromagnetic resistive losses generated in the nanoparticles are considered as the only heat source. To solve the heat equation, we have assumed that the electromagnetic cycle time is short compared with the thermal time scale (adiabatic assumption). To take into account the heat dissipation in our simulation region, we used a heat flux node across the outer boundaries by considering a heat transfer coefficient dependent on the geometry and ambient flow conditions.

Govorov's model -one of the most efficient ways to understand photothermal effects in nanoplasmonic particles- has been used as an initial gauge tool. This model solves the aforementioned heat equation for a simple spherical geometry, where the steady-state temperature as a function of the radial distance  $r$ , can be derived analytically, obtaining the well-known expression

$$\Delta T(r) = \frac{V_{NP}Q}{4\pi k_0 r} \quad (2)$$

where  $V_{NP}$  is the nanoparticle volume,  $R_{NP}$  the nanoparticle radius,  $r > R_{NP}$  is the radial distance, and  $k_0$  is the thermal conductivity of the surrounding medium. Here, the heat losses  $Q$  in the particle can be obtained by means of the Joule effect expression

$$Q(\vec{r}) = \langle \vec{J}(\vec{r},t) \cdot \vec{E}(\vec{r},t) \rangle \quad (3)$$

where  $\vec{E}$  is the electric field inside the sphere,  $\vec{J}$  is the current density,  $\vec{r}$  is the position vector, and  $t$  is time. In most cases, intricate nanoparticle geometries prevent an analytical solution of the scattering problem in the nanoparticle. However, for a spherical nanoparticle, the electric field inside the sphere can be obtained

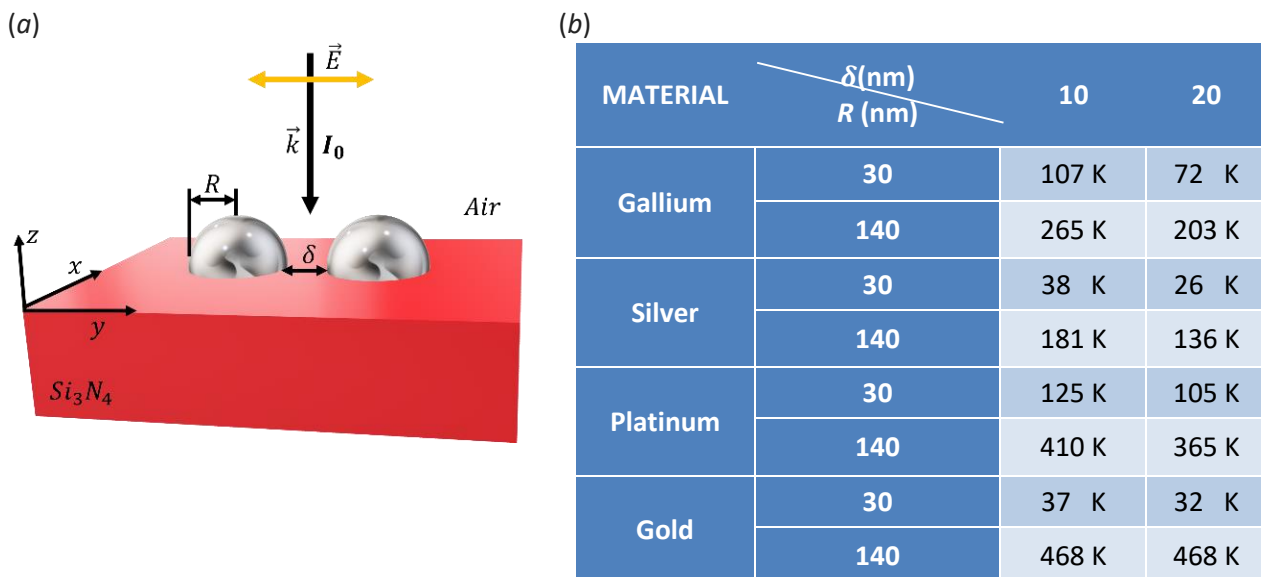
by means of the quasi-static approximation, where the sphere size is much smaller than the excitation wavelength. Under this approximation, the  $Q$  value can be obtained as

$$Q = \frac{\omega}{8\pi} E_0^2 \left| \frac{3\epsilon_0}{2\epsilon_0 + \epsilon_{NP}} \right|^2 \Im[\epsilon_{NP}] \quad (4)$$

where  $\omega$  is the angular frequency,  $E_0$  the electric field amplitude,  $\epsilon_0$  is the surrounding medium permittivity and  $\epsilon_{NP}$  the permittivity of the nanoparticle.

So far, we have studied the thermoplasmonic response of a dimer of hemispherical nanoparticles of different materials for different radius and gap distances (Fig. 13a). The particles are illuminated at normal incidence with a y-axis polarized beam of approximately  $150 \text{ mW}/\mu\text{m}^2$ . This study includes hemisphere radii of 30 and 140 nm, separated 10 and 20 nm, the temperature increase being measured in the proving point located at the geometrical center of the dimer. The phenomenology of the results has been analysed based on the aforementioned Govorov's theory.

According to Fig. 13b, the temperature increase with the particle radius for all materials. This is in agreement with Govorov's model (eq.(2)), reaching a maximum temperature at the particle surface. Also, the temperature reduces as we increase the interparticle distance, which again, is expected considering the temperature dependence with the distance to the particle surface, in sight of equation 1.



**Figure 13.-** (a) System composed by two hemispheres resting on a  $\text{Si}_3\text{N}_4$  substrate illuminated with a y-axis polarized wave at  $\lambda = 470 \text{ nm}$  and a power density of  $I_0 \approx 150 \text{ mW}/\mu\text{m}^2$ . The radii of the hemispheres are  $R=30$  and  $140 \text{ nm}$  and the gap  $\delta=10$  and  $20 \text{ nm}$ . The considered materials for hemispheres are gallium, silver, platinum and gold. (b) table containing the temperature increase calculated for all the previous cases.

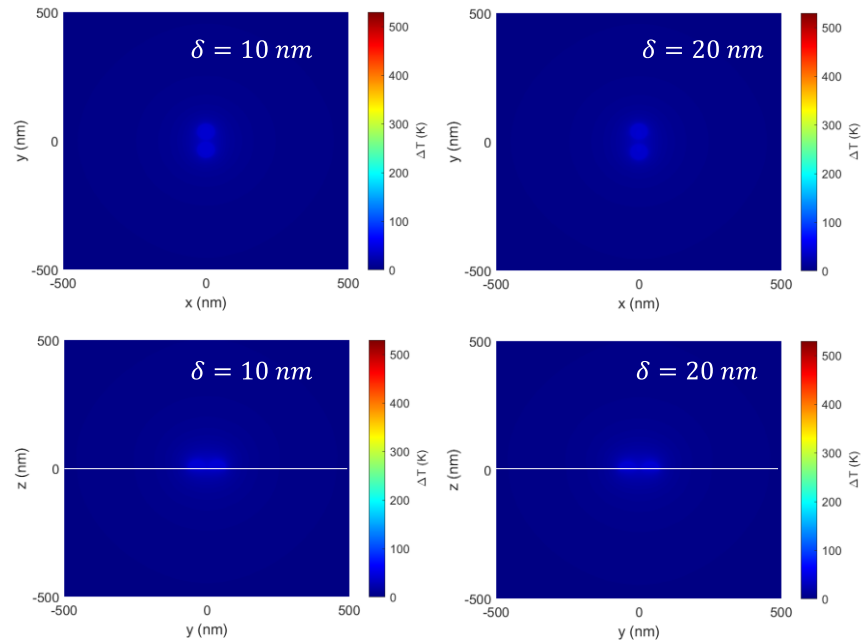
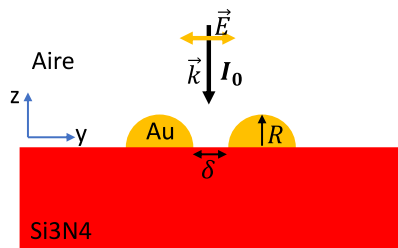
The temperature-increase ( $\Delta T$ ) spatial distributions for each of the dimer configuration are shown below. In order to emphasize the increment of  $\Delta T$  when increasing the radius of the hemispheres (from 30 to 140 nm), the maps for various metals are plotted in the same scale.

- Au dimer**

$$R = 30 \text{ nm}$$

$$I_0 \approx 1,5 \cdot 10^{11} \text{ W/m}^2$$

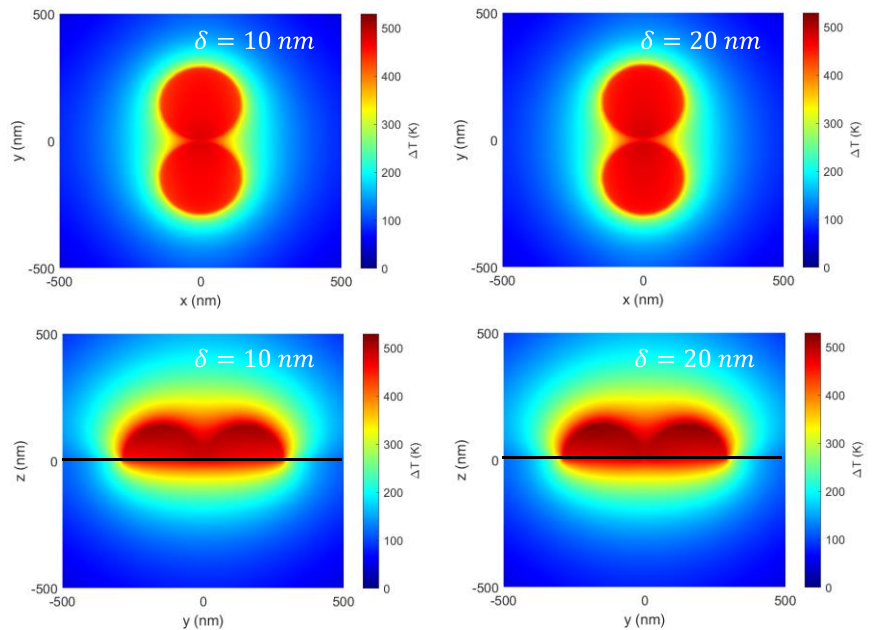
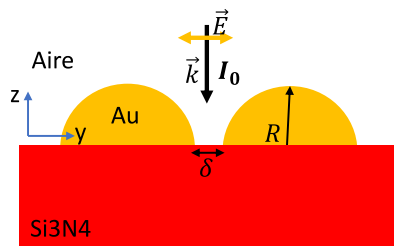
$$\lambda \approx 470 \text{ nm}$$



$$R = 140 \text{ nm}$$

$$I_0 \approx 1,5 \cdot 10^{11} \text{ W/m}^2$$

$$\lambda \approx 470 \text{ nm}$$

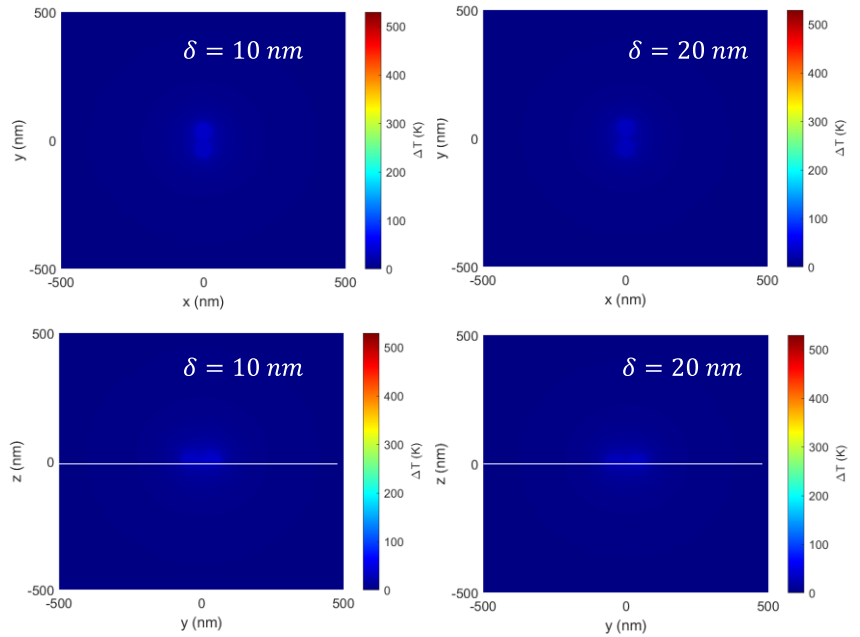
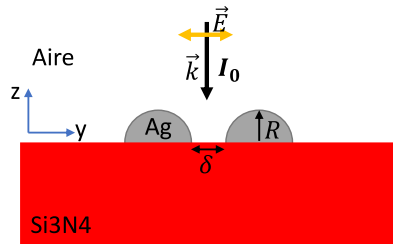


- Ag dimer

$$R = 30 \text{ nm}$$

$$I_0 \approx 1,5 \cdot 10^{11} \text{ W/m}^2$$

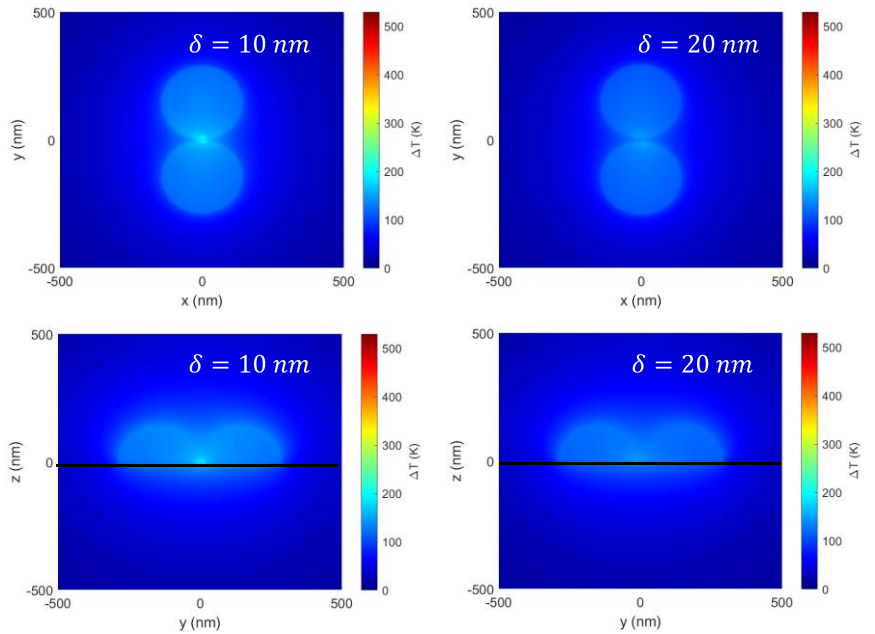
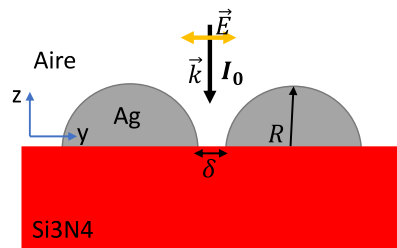
$$\lambda \approx 470 \text{ nm}$$



$$R = 140 \text{ nm}$$

$$I_0 \approx 1,5 \cdot 10^{11} \text{ W/m}^2$$

$$\lambda \approx 470 \text{ nm}$$

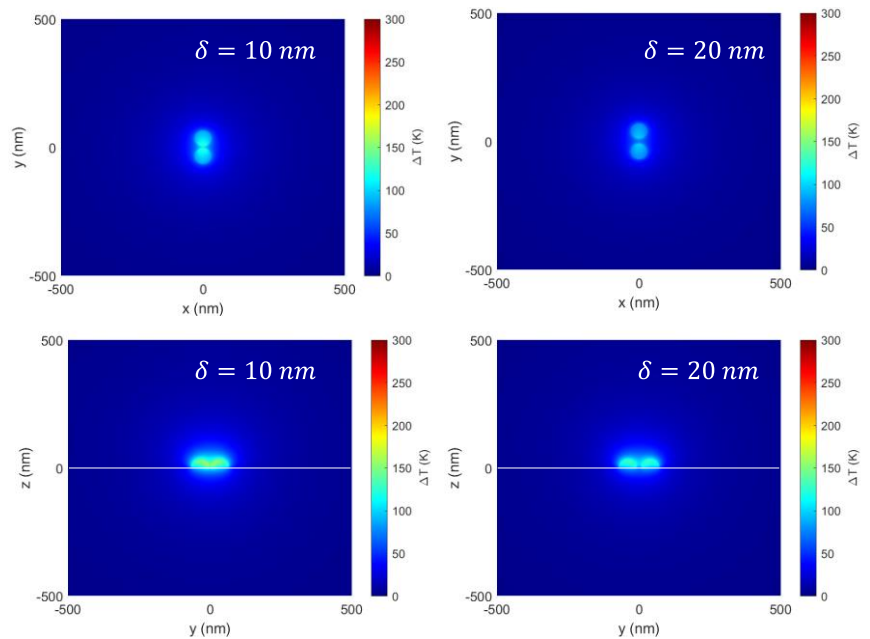
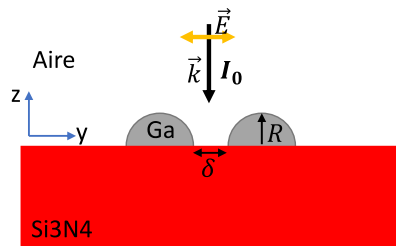


- Ga dimer

$$R = 30 \text{ nm}$$

$$I_0 \approx 1,5 \cdot 10^{11} \text{ W/m}^2$$

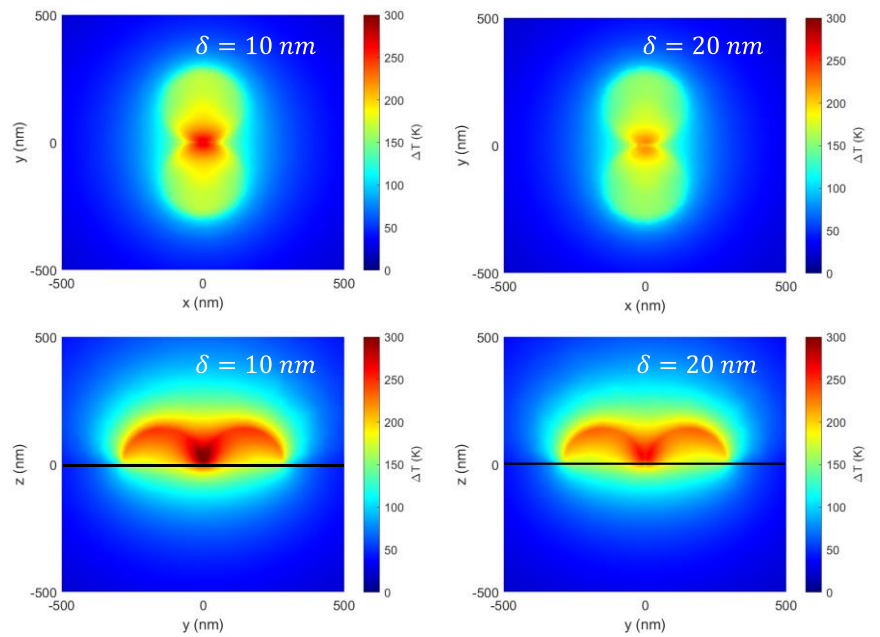
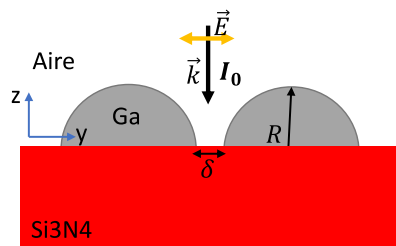
$$\lambda \approx 470 \text{ nm}$$



$$R = 140 \text{ nm}$$

$$I_0 \approx 1,5 \cdot 10^{11} \text{ W/m}^2$$

$$\lambda \approx 470 \text{ nm}$$



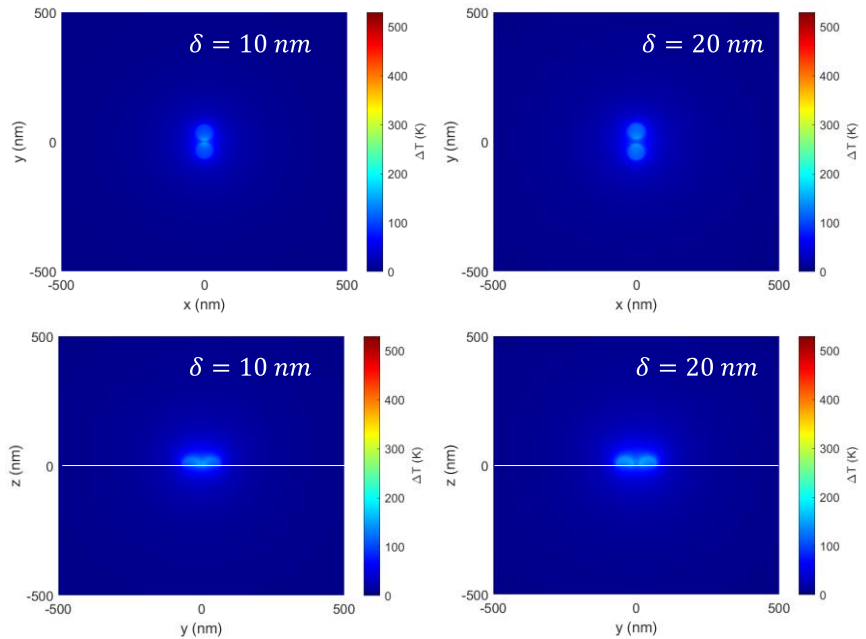
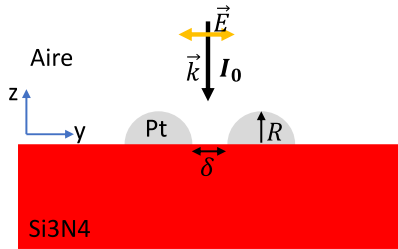


- Pt dimer

$$R = 30 \text{ nm}$$

$$I_0 \approx 1,5 \cdot 10^{11} \text{ W/m}^2$$

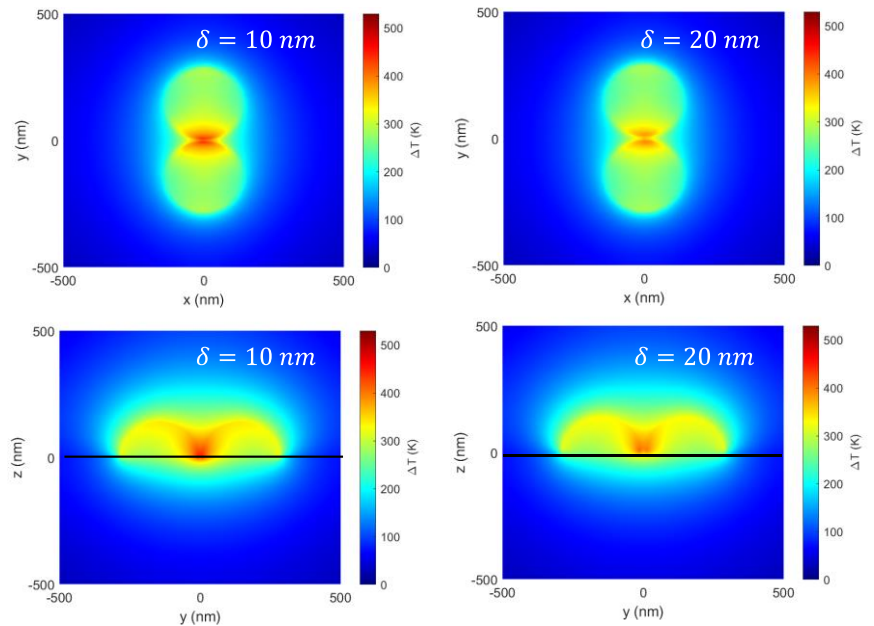
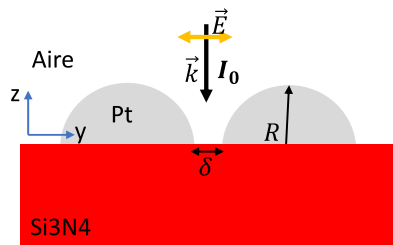
$$\lambda \approx 470 \text{ nm}$$



$$R = 140 \text{ nm}$$

$$I_0 \approx 1,5 \cdot 10^{11} \text{ W/m}^2$$

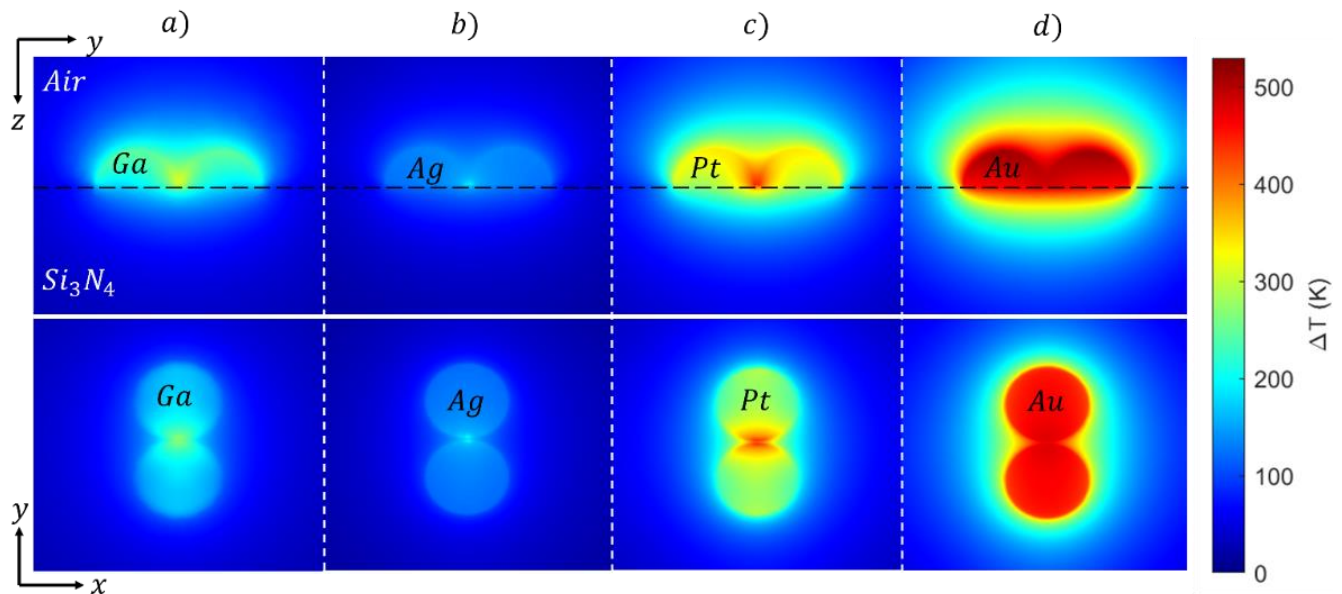
$$\lambda \approx 470 \text{ nm}$$



The differences between the plasmonic metals are summarized in Fig. 14, for the geometrical parameters that provide the highest temperature increase, i.e., the largest hemisphere radius and the smallest gap. It can be clearly seen that the highest temperature increment is obtained by Au nanoparticles, reaching temperatures up to 468 K approximately; silver is the worst thermal generator leading to an increment of temperature of approximately 180K. This different behavior can be explained considering the important role of the nanoparticle permittivity on the thermal response modelled in equation 3 and the effects that geometry and substrate have on the spectral thermal response. Although for a single spherical nanoparticle, the order of the heating capability would be gold, silver, platinum and gallium, the thermal spectrum for the



configuration shown in Fig.13a is redshifted due to the hemisphere on substrate geometry and to the substrate effect, leading to the results in Fig. 14.



**Figure 14.-** Temperature maps for two metallic hemispheres separated  $\delta = 10$  nm on a  $Si_3N_4$  substrate illuminated with a y-axis polarized wave at  $\lambda = 470$  nm: a) gallium, b) silver, c) platinum and d) gold.

## 5. Plasmonics vs Thermoplasmonics

In this section, the plasmonic performance of the Ga dimer nanoantenna is compared with temperature simulations to analyze if there are worthy correlations to be considered. For this purpose, the temperatures obtained for gallium, silver, platinum and gold for gaps of 10 and 20 nm, and radii 30 and 140 nm are compared in terms of the enhancement obtained in each case for the wavelength of interest (470nm) (see Fig. 15).

## Enhancement

MATERIAL	$\delta$ (nm)	10	20
	R (nm)		
Gallium	30	44.786	10.397
	140	51.71	13.37
Silver	30	0.786	0.105
	140	6.178	1.254
Platinum	30	34.916	7.955
	140	40.544	11.770
Gold	30	0.781	0.5941
	140	0.817	0.5586

## Temperature

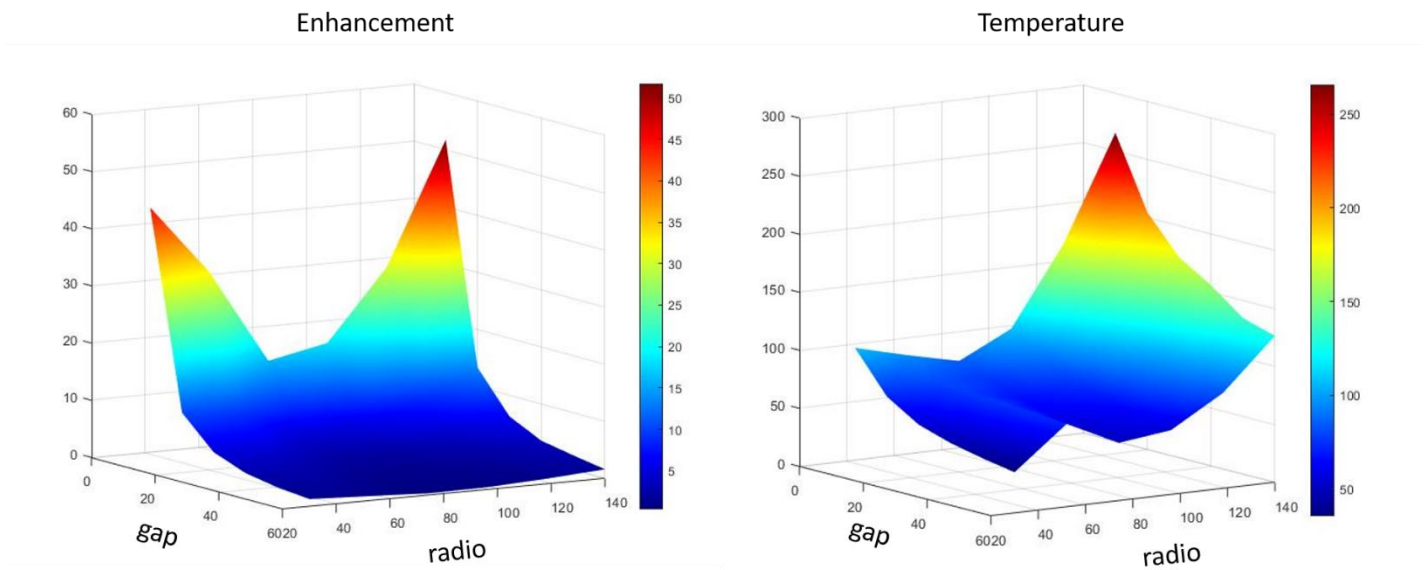
MATERIAL	$\delta$ (nm)	10	20
	R (nm)		
Gallium	30	107 K	72 K
	140	265 K	203 K
Silver	30	38 K	26 K
	140	181 K	136 K
Platinum	30	125 K	105 K
	140	410 K	365 K
Gold	30	37 K	32 K
	140	468 K	468 K

**Figure 15.-** Comparison of the enhancement generated by different nanoantenna, radius and gaps, with the temperature achieved in each case. The materials are; platinum, silver, gold and gallium. The gaps are: 10 and 20 nm. The radii are: 30 and 140 nm. Those magnitudes are described for a wavelength of 470 nm.

Considering the wavelength of 470 nm, the highest electromagnetic enhancement is obtained for the gallium dimer nanoantenna given the LSPR matching the wavelength of 470 nm due to the optimal tuning of the radius of the nanoparticles. For gold, very low electromagnetic enhancements are obtained because there is no LSPR matching the 470nm wavelength, but a high temperature could be generated (over 400K) because of the interband absorption in gold.

In the case of Ga dimer nanoantenna, we investigated in more detail the effect of the dimer gap between 10 and 60 nm and of the nanoantenna radius from 30 and 140 nm on both the electromagnetic enhancement and the temperature increment. The results are shown in Fig 16. The electromagnetic enhancement is high for small gaps, and for both radii of 30 and 140 nm, as explained previously. Conversely, the temperature increment is relevant only for small gaps and for the 140 nm radius, since the temperature increases with the size of the nanoparticles according to Govorov's model.

Thus, if thermoplasmonic effects are used for phase transformation between amorphous and crystalline, Ga nanoantennas of larger size are required, in our case 140nm. For the wavelength of interest (470 nm) and a gap of 10 nm, a temperature increment of 265°C can be produced.

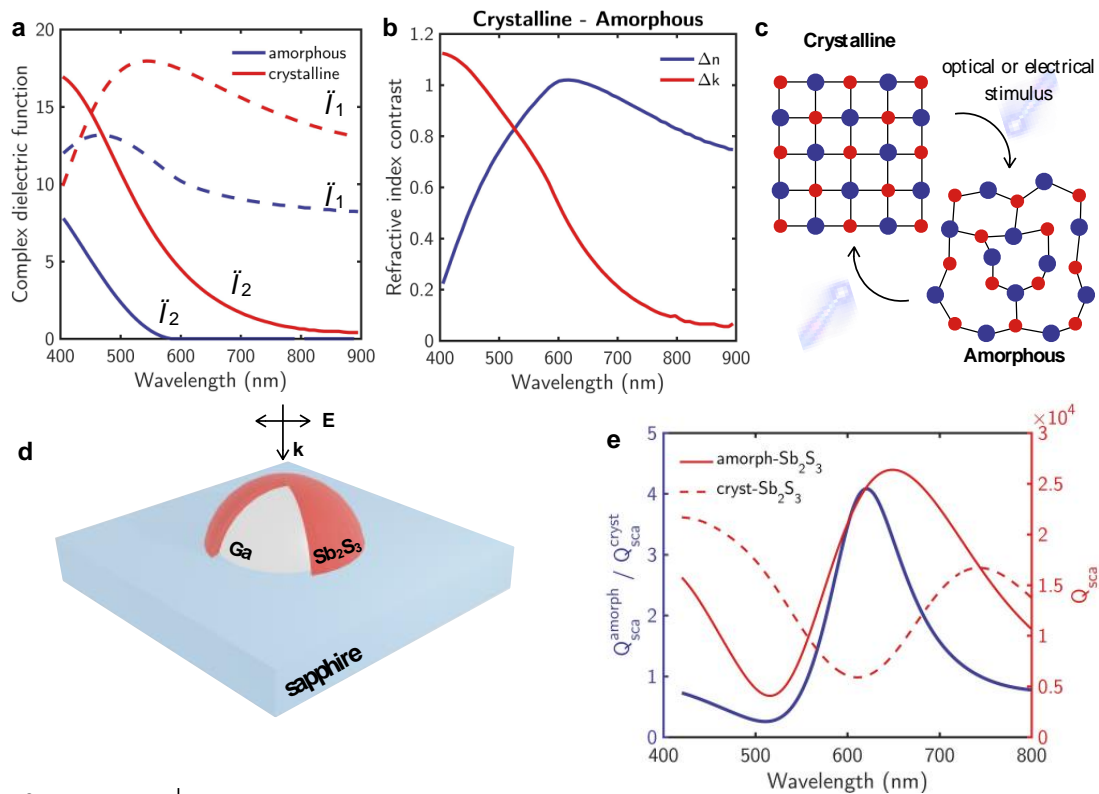


**Figure 16.-** Comparison between electromagnetic enhancement and temperature of Ga nanoantennas for gap values in the dimer ranging between 10 and 60 nm, radii from 30 to 140 nm and at a wavelength of 470 nm.

## 6. Core-Shell Reconfigurable Nanoantennas

In this section, we present some preliminary calculations on a new type of reconfigurable Ga nanoantenna. It consists of a liquid Ga NP core with a PCM shell and deposited on a dielectric substrate (e.g. the  $\text{Si}_3\text{N}_4$  waveguide). The idea behind this design consist in the modulation of the scattering efficiency of the nanoantenna by changing the dielectric function of the PCM shell through its crystalline-amorphous transition. As PCM for these calculations we have chosen, as an example, another emerging alternative PCM at optical frequencies that will be deposited and considered in PHEMTRONICS, i.e.,  $\text{Sb}_2\text{S}_3$ .  $\text{Sb}_2\text{S}_3$  has a wide band gap of  $2.05 \pm 0.05$  and  $1.72 \pm 0.05$  eV in the amorphous and crystalline states, and exhibiting a large refractive index contrast in the visible during the structural phase transition. Therefore, PCM  $\text{Sb}_2\text{S}_3$  can be coupled to conventional passive plasmonic nanoantennas with LSPRs at optical frequencies to generate hybrid structures with a reconfigurable plasmonic response in the visible. To illustrate this, Figure 17a shows the complex dielectric function of  $\text{Sb}_2\text{S}_3$ . Figure 17b shows the refractive index contrast ( $\Delta n = n_{\text{cryst}} - n_{\text{amorph}}$  and  $\Delta k = k_{\text{cryst}} - k_{\text{amorph}}$ ) between the amorphous and crystalline phases. The maximum value of  $\Delta n = 1$  is produced at 600 nm while keeping a relative low modulation of the extinction coefficient,  $k$ , (i.e. low value of  $\Delta k$ ). Figure 17c illustrates the fact that the transformation between crystalline and amorphous phases has been proven to be reversible and it can be triggered by either electrical or optical stimuli.<sup>28</sup> This process leads to the possibility of forming hybrid structures, for instance, core-shell nanospheres, to tailor the plasmonic

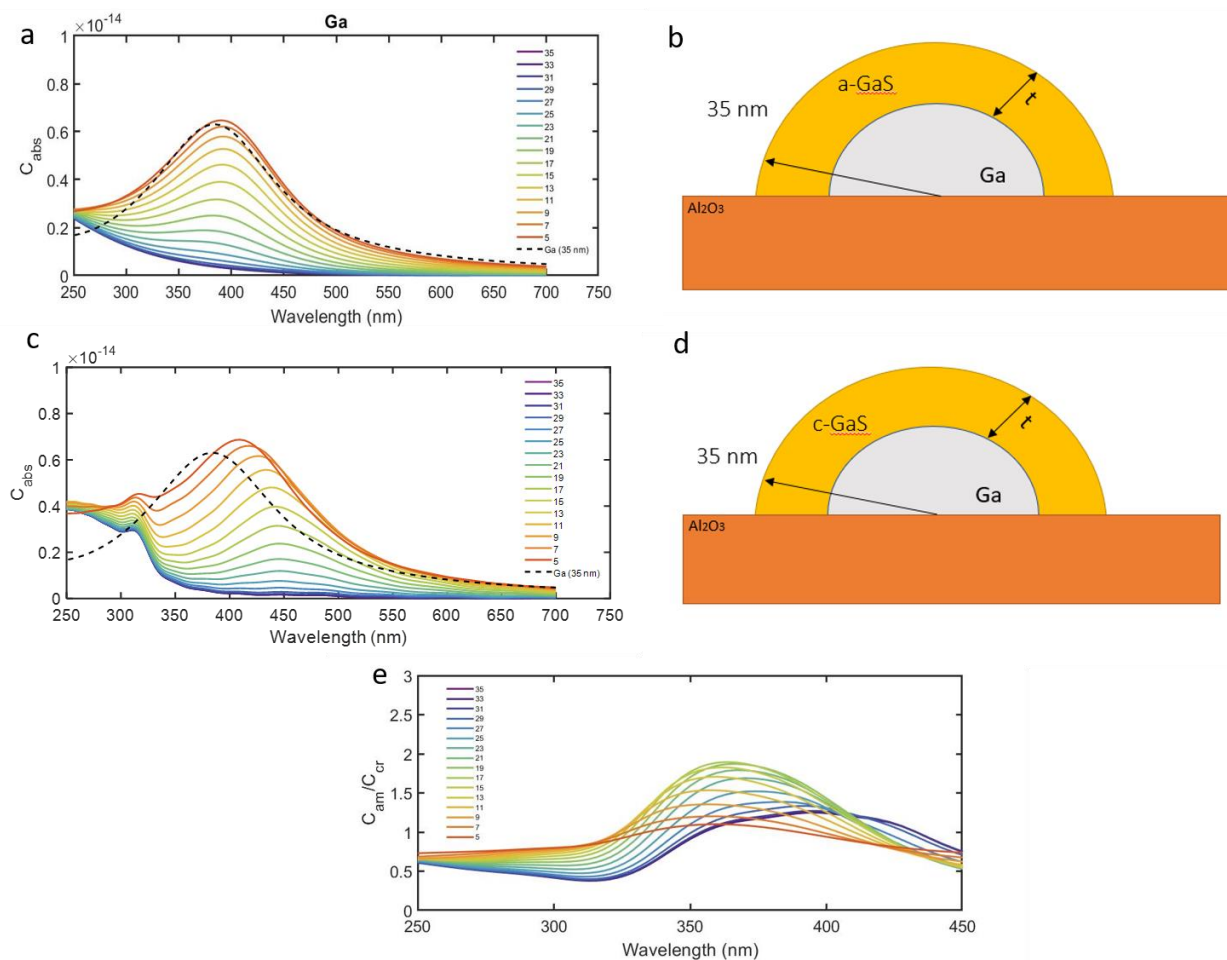
response of the system. Figure 17d shows the example of a Ga-Sb<sub>2</sub>S<sub>3</sub> core-shell hemispherical nanoparticle on a dielectric substrate ( $R_{\text{core}} = 50$  nm and  $R_{\text{total}} = 75$  nm) whose scattering efficiency can be modulated by the amorphous-to-crystalline phase transition of the Sb<sub>2</sub>S<sub>3</sub> shell. Specifically, in Fig. 17e, the right axis shows both the individual spectral scattering efficiencies,  $Q_{\text{sca}}$ , of the Ga-core/amorphous- Sb<sub>2</sub>S<sub>3</sub>-shell and of the Ga-core/crystalline- Sb<sub>2</sub>S<sub>3</sub> core-shell, while the left- axis shows the ratio of scattering efficiencies of the system upon phase transition. Noteworthy, at the resonant wavelength, and by changing the phase of the Sb<sub>2</sub>S<sub>3</sub>, it is possible to enhance the value of  $Q_{\text{sca}}$  by a factor 4.5.



**Figure 17.** (a) Real (solid line) and imaginary part (dashed line) of the complex dielectric function of amorphous and crystalline Sb<sub>2</sub>S<sub>3</sub>. (b) Refractive index contrast ( $\Delta n$  and  $\Delta k$ ) between amorphous and crystalline Sb<sub>2</sub>S<sub>3</sub>. (c) Scheme of the crystalline to amorphous reversible transformation. (d) Scheme of the system in which the plasmonic simulations have been performed: Ga-Sb<sub>2</sub>S<sub>3</sub> core-shell hemisphere supported on a dielectric substrate and illuminated at normal incidence. (e) Scattering efficiency ( $Q_{\text{sca}}$ ) of a Ga-Sb<sub>2</sub>S<sub>3</sub> core-shell hemisphere located on a sapphire substrate with total and core radii of 75 and 50 nm, respectively. Left axis represents the ratio between  $Q_{\text{sca}}$  of the Au-amorph-Sb<sub>2</sub>S<sub>3</sub> and that of Ga-cryst-Sb<sub>2</sub>S<sub>3</sub> core-shells. Right axis represents the individual  $Q_{\text{sca}}$  spectra of the Ga-amorph-Sb<sub>2</sub>S<sub>3</sub> (solid line) and that of Ga-cryst-Sb<sub>2</sub>S<sub>3</sub> (dashed line) core-shells, respectively.

Similarly, calculations have been performed using GaS as PCM for the shell in the core-shell nanostructure configuration. In this case, the total radius of the core-shell nanostructure was set to 35 nm with an increasing thickness of the GaS shell that consumes the *I*-Ga core. Figure 18a shows the absorption cross-section of Ga NPs with a shell of amorphous GaS (a-GaS) whose thickness is varied from 5 to 35 nm (Fig. 18b). As the shell thickness is increased, the resonance at 400 nm is monotonically quenched. In Figure 18c, the absorption

cross-section is analyzed for the crystalline (c-GaS) shell. Also in this case, the Ga-core LSPR is quenched with the increase of the GaS shell thickness. This behavior can be explained considering the reduction of the metallic component in the core-shell structure as the thickness of the dielectric shell increases. For both a-GaS and c-GaS shells, with increasing shell thickness, the LSPR is red-shifted. This red-shift is larger for c-GaS because of its higher refractive index when compared to a-GaS. For comparison purposes, the absorption cross section of a Ga NP without the GaS shell is plotted with a black dashed line. In Fig 18e, the absorption cross-sections ratio between both GaS phases is shown in order to explore the modulation on the absorption cross-section of the system that can be achieved by switching the GaS phase. A ratio as high as 1.9 is achieved for a shell thickness of 17 nm.



**Figure 18.** (a) Absorption cross-section of Ga NPs of radius 35 nm with a shell of amorphous GaS whose thickness is varied from 5 to 35 nm. (b) Scheme of the core(Ga)-shell(a-GaS) NPs. (c) Absorption cross-section of Ga NPs of radius 35 nm with a shell of crystalline GaS whose thickness is varied from 5 to 35 nm. (d) Scheme of the core(Ga)-shell(c-GaS) NPs. (e) Ratio of the absorption cross sections between the two configurations shown in a) and c) for the amorphous and crystalline phases of the GaS shell, respectively.

## 7. Plasmon-Coupling for Reconfigurable Photodetectors

One of the technological objectives of PHEMTRONICS is to demonstrate adaptive waveguide integrated switchable multi-detectors array.

In this section, we propose and analyze some initial and basic configurations based on surface plasmon coupling through metallic gratings to waveguides made of the PCMs proposed in this project. In particular, calculations are performed using  $\text{Sb}_2\text{S}_3$  as the substrate/waveguide since one of the partners (NANOM-MEMS) is expert in the fabrication and treatment of this sort of material. Its optical properties were provided by ellipsometric measurements from PHEMTRONICS partners.  $\text{Sb}_2\text{S}_3$  shows a light induced transition between the two phases of amorphous and crystalline.

In this deliverable, preliminary configurations are considered in order to analyze the different electromagnetic behavior of both phases of  $\text{Sb}_2\text{S}_3$ . Those configurations consist in periodic gratings of  $\text{Sb}_2\text{S}_3/\text{Au}$ .

The simulations have been performed considering:

- A discrete number of grooves. Specifically, the number of grooves has been fixed to 100.
- Incident electric field polarized perpendicularly to the groove direction (p-polarization).
- Normal incidence. Although gratings show strong angular dependence, normal incidence is enough to understand the contrast in electromagnetic behavior between amorphous and crystalline phases.
- Gaussian beam to mimic the laser illumination in a real experiment in the laboratory.

Surface plasmons are coherent delocalized electron oscillations that exist at the interface between any two materials where the real part of the dielectric function changes sign across the interface (e.g. a metal-dielectric interface). Plasmons can be excited by electrons, phonons, or photons. We are interested in photon excitation but plasmons cannot be excited on a planar metallic-dielectric interface by direct illumination since photons have no enough momentum to excite a surface plasmon wave. An extra momentum must be added to get plasmonic excitation. For instance, this can be provided by a periodic grating. The equation obeying the coupling of incident photons to a surface plasmon through a periodic grating is given by<sup>28</sup>

$$\lambda = \frac{P}{m} \left( \pm \sqrt{\frac{\epsilon_1 \epsilon_2}{\epsilon_1 + \epsilon_2}} - \sqrt{\epsilon_1} \sin(\theta) \right) \quad (5)$$

where  $\lambda$  is the wavelength of the generated plasmon,  $P$  is the period of the grating,  $m$  is the plasmon order,  $\epsilon_1$  is the real part of the dielectric function of the dielectric medium,  $\epsilon_2$  is the real part (negative) of the metal and  $\theta$  the incident angle. For all of these simulations, plasmons of first order ( $m=1$ ), which is the most efficient in terms of energy, are considered.

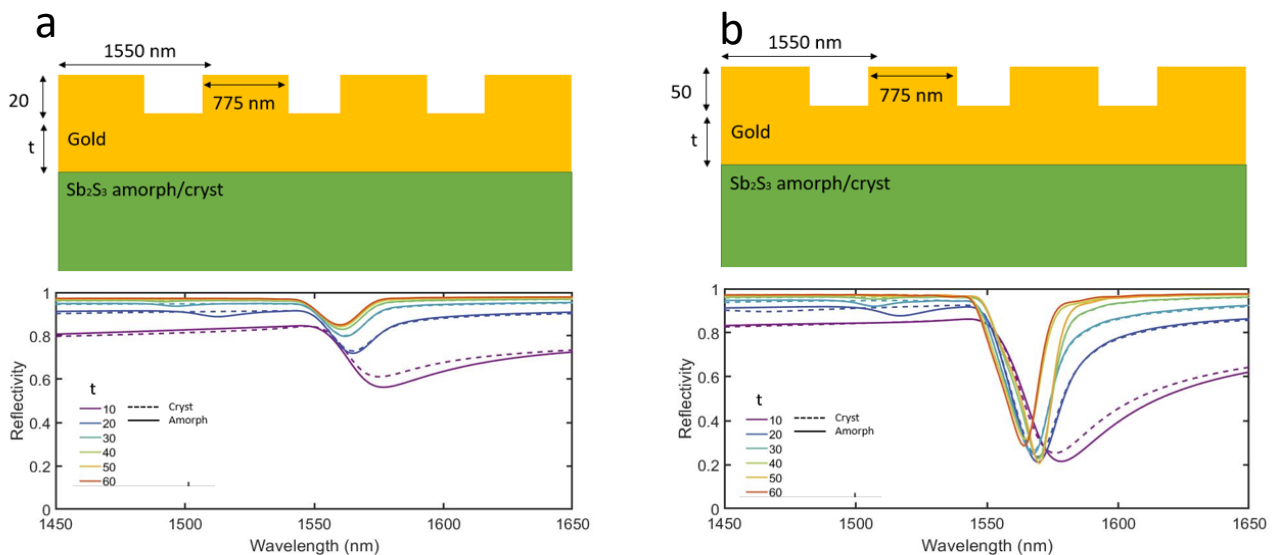


In this deliverable, the grating will be located on a PCM substrate ( $\text{Sb}_2\text{S}_3$  in our case which in turn can act as a waveguide) and the coupling of the generated plasmon by the grating with the substrate will be analyzed by considering different configurations as it is described in the following.

In general, the main parameters characterizing a diffraction grating are: the duty cycle ( $D$ ), the height of the grooves ( $d$ ), the period ( $P$ ), the polarization (perpendicular to the grooves ( $p$ )) and the incident angle ( $\theta$ ). The duty cycle has been considered 0.5 in all the configurations. Conversely, two different periods have been considered: near 1550 nm for air-gold interfaces (Figs 19, 20 and 21), and 530 nm for  $\text{Sb}_2\text{S}_3$ -gold interface (Fig 22). The reason of these periods is the generation of a plasmon resonance in the third telecom window. For an air-gold interface, plasmon resonance is generated at a wavelength very near to the period. Conversely, for the  $\text{Sb}_2\text{S}_3$ -gold interface, due to the high index refractive index of the PCM, the period should be reduced in order to guarantee plasmon resonance at this window.

Figures. 19, 20 and 21 shows configurations based on the excitation of surface plasmons at the air-gold interface.

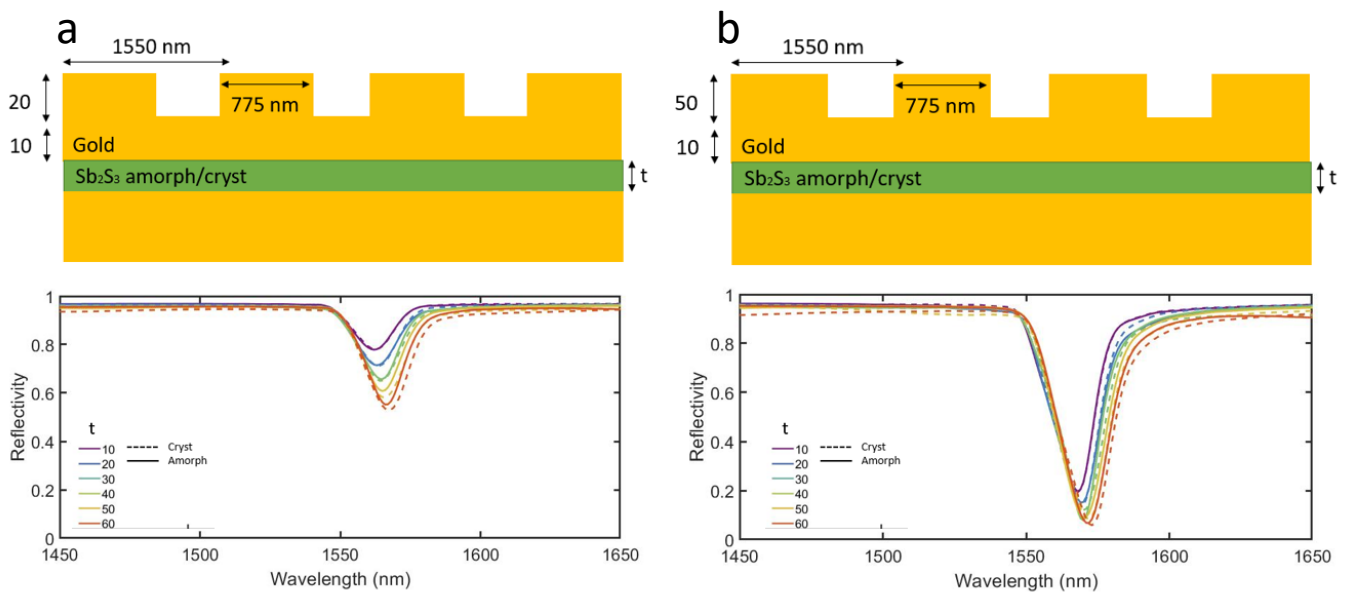
In Figure 19, we consider a gold grating on a  $\text{Sb}_2\text{S}_3$  substrate with a period of 1550 nm. In this configuration, we choose two different layouts depending on the height of the groove: 20 nm (Fig. 19a) and 50 nm (Fig. 19b).



**Figure 19.** (a) Reflectance spectrum for a gold grating on a  $\text{Sb}_2\text{S}_3$  substrate with a period of 1550 nm, duty cycle 0.5, normal incidence, p-polarized light, gaussian beam, a height of the grooves of 20 nm and for a variable gold thickness  $t$  from 10 to 60 nm. Continuous line represents amorphous state and dashed line, crystalline. (b) Reflectance spectrum for a gold grating on a  $\text{Sb}_2\text{S}_3$  substrate with a period of 1550 nm, duty cycle 0.5, normal incidence, p-polarized light, gaussian beam, a height of the grooves of 50 nm and for a variable gold thickness  $t$  from 10 to 60 nm. Continuous line represents amorphous state and dashed line, crystalline.

For both groove's heights considered here, the thickness of the gold film,  $t$ , is varied from 10 to 60 nm. Reflectance spectra were calculated for amorphous and crystalline states of the  $\text{Sb}_2\text{S}_3$  substrate as a function of the thickness of the Au layer. In the figure, continuous lines represent amorphous whereas dashed lines represent the crystalline phase. Only for the thinner Au layer, small differences in reflectance spectra can be appreciated when switching between the crystalline and amorphous phases. As  $t$  is increased, considering Au's *skin depth*, more light is absorbed in the Au layer and does not reach the  $\text{Sb}_2\text{S}_3$ . Consequently, for high  $t$  values, the same reflectance spectra is achieved independently of  $\text{Sb}_2\text{S}_3$  phase.

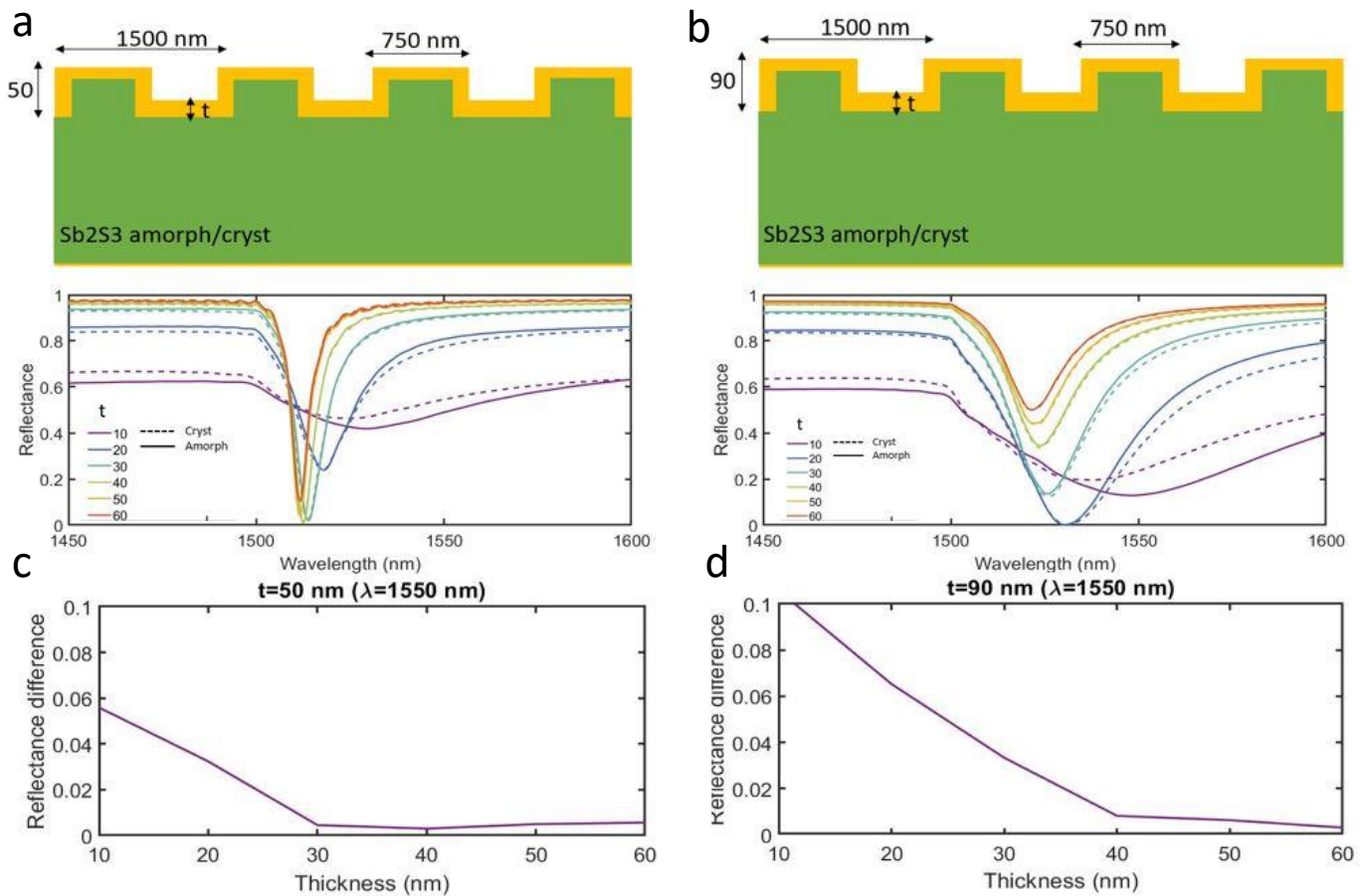
Another studied configuration based on the excitation of surface plasmons at the air-gold interface is shown in Fig. 20. Again, the period was set to 1550 nm and two different groove heights were considered: 20 (Fig. 20a) and 50 nm (Fig. 20b). In this case, the PCM  $\text{Sb}_2\text{S}_3$  layer is located between a gold grating and a gold substrate. The thickness of gold layer is fixed to 10 nm, and the thickness of  $\text{Sb}_2\text{S}_3$  is varied from 10 to 60 nm. This configuration was proposed aiming the excitation of a second surface plasmon propagating at the gold- $\text{Sb}_2\text{S}_3$  interface. However, as it can be seen in the reflectance spectrum, a second plasmon is not produced due to the high contrast between air and the PCM dielectric function. Reflectivity curves are very similar for both of the groove's heights considered as shown in Figs. 20a,b independently of the phase of the  $\text{Sb}_2\text{S}_3$  layer.



**Figure 20.** (a) Reflectance spectrum for a  $\text{Sb}_2\text{S}_3$  layer located between a gold grating and a gold substrate with a period of 1550 nm, duty cycle 0.5, normal incidence, p-polarized light, Gaussian beam, a height of the grooves of 20 nm and for a variable  $\text{Sb}_2\text{S}_3$  thickness  $t$  from 10 to 60 nm. Continuous line represents amorphous state and dashed line, crystalline. (b) Reflectance spectrum for a  $\text{Sb}_2\text{S}_3$  layer located between a gold grating and a gold substrate with a period of 1550 nm, duty cycle 0.5, normal incidence, p-polarized light, Gaussian beam, a height of the grooves of 50 nm and for a variable  $\text{Sb}_2\text{S}_3$  thickness  $t$  from 10 to 60 nm. Continuous line represents amorphous state and dashed line, crystalline. In both cases the thickness of the gold layer supporting the gold grooves is 10 nm.



An additional investigated plasmonic configuration for phase-change photodetectors based on the excitation of surface plasmons at air-gold interface is shown in Fig. 21. It consists in a  $\text{Sb}_2\text{S}_3$  grating covered by a thin Au layer. In this configuration, the period is fixed to 1500 nm. Two different heights of the grooves have been studied: 50 nm (Fig. 21a) and 90 nm (Fig. 21b). The reflectance spectra considering different thickness  $t$  of the gold layer ranging from 10 to 60 nm and both  $\text{Sb}_2\text{S}_3$  phases (amorphous – continuous lines and crystalline – dashed lines) are shown in Figs. 21a,b. The largest reflectance contrast in switching between the  $\text{Sb}_2\text{S}_3$  phases is generated for the lowest thickness of the Au layer. In order to study in more detail this phenomenon, the reflectance difference ( $R_{\text{cryst}} - R_{\text{amorph}}$ ) between  $\text{Sb}_2\text{S}_3$  phases at the wavelength of 1550 nm is plotted in Figs 21c,d as a function of the gold thickness for both grooves heights. A clear modulation in the reflectance spectra when switching from the crystalline and amorphous phases is observed only for the thinnest Au thickness. Noteworthy, the values of  $R_{\text{cryst}} - R_{\text{amorph}}$  are increased by increasing the groove height.



**Figure 21.** (a) Reflectance spectrum for a  $\text{Sb}_2\text{S}_3$  grating covered by a gold layer with a period of 1500 nm, duty cycle 0.5, normal incidence, p-polarized light, Gaussian beam, a height of the grooves of 50 nm and for a variable gold thickness  $t$  from 10 to 60 nm. Continuous line represents amorphous state and dashed line, crystalline. (b) Reflectance spectrum for a  $\text{Sb}_2\text{S}_3$  grating covered by a gold layer with a period of 1500 nm, duty cycle 0.5, normal incidence, p-polarized light, Gaussian beam, a height of the grooves of 90 nm and for a variable gold thickness  $t$  from 10 to 60 nm. Continuous line represents amorphous state and dashed line, crystalline. (c) Reflectance variation between amorphous and crystalline phases for a wavelength of 1550 nm and for configuration (a). (d) Reflectance variation between amorphous and crystalline phases for a wavelength of 1550 nm and for configuration (b).

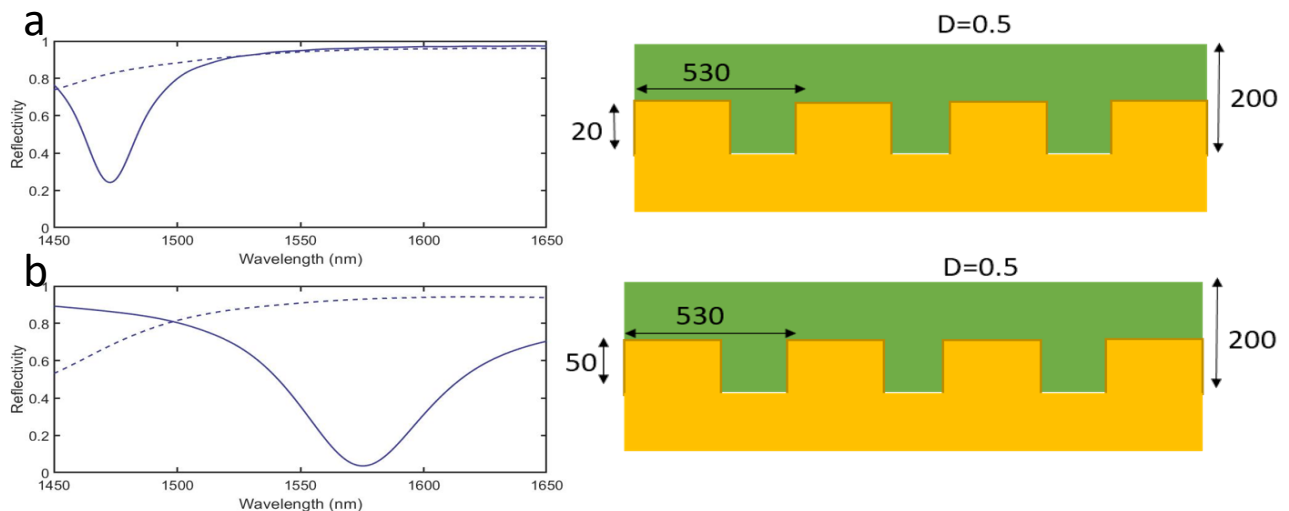
Thus, for all the plasmonic-phase change configurations in Figures 19, 20, 21, we can conclude that the electromagnetic behavior of those gold-grating based configurations is very similar leading to a low modulation of the properties of the generated surface plasmons. This is due to the light absorbed in the Au layer and not efficiently reaching the PCM to activate its phase transformation.

**Therefore, these configurations are not suitable to achieve a modulation of the surface plasmon properties among switching between amorphous and crystalline phases of  $\text{Sb}_2\text{S}_3$ .**

**Noteworthy, this conclusion can be extended to other PCMs, e.g. GaS, when exploited in the above same configurations.**

In figure 22 we propose a more effective configuration based on the PCM covering the gold grating. The thickness of the PCM layer,  $\text{Sb}_2\text{S}_3$  in this case, is set to 200 nm, the period to 550 nm and the height of the grooves to 20 nm (Fig. 22a) and 50 nm (Fig. 22b), respectively. The refractive index of  $\text{Sb}_2\text{S}_3$ , in the amorphous phase, is approximately 3 times higher than that of air; hence, the period could be reduced approximately by a factor three to generate a plasmon resonance of first order in the third telecom window.

In this configuration, the difference in the contrast of the spectral reflectance between the crystalline and amorphous  $\text{Sb}_2\text{S}_3$  layers is significant. This can be rationalized by considering that now the surface plasmon is excited at the PCM – interface. Therefore, the surface plasmon electromagnetic behavior depends directly on the optical properties of  $\text{Sb}_2\text{S}_3$ .



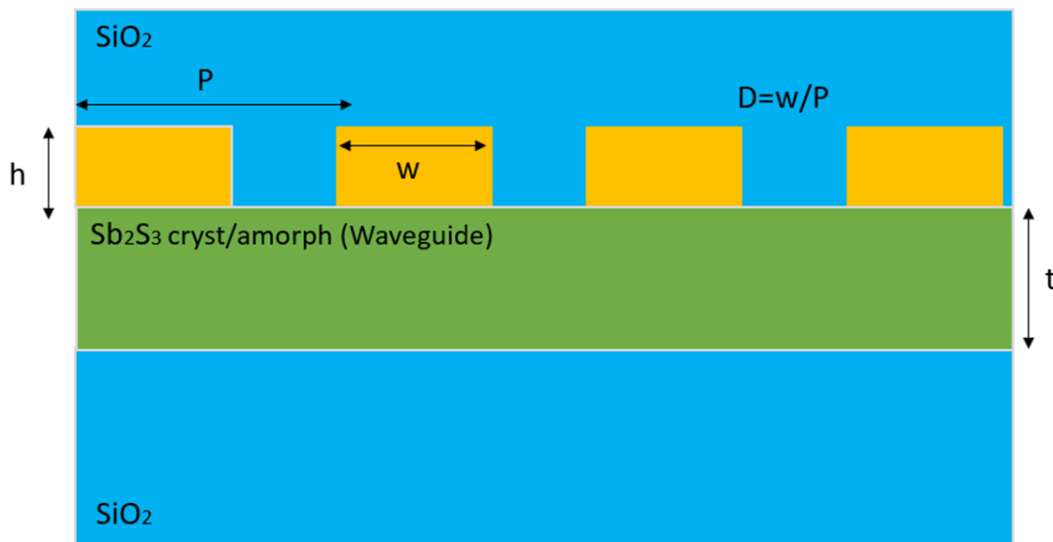
**Figure 22.** (a) Reflectance spectrum for a  $\text{Sb}_2\text{S}_3$  layer on top of a gold grating with a period of 1550 nm, duty cycle 0.5, normal incidence, p-polarized light, Gaussian beam, a height of the grooves of 20 nm. The thickness of  $\text{Sb}_2\text{S}_3$  layer is 200 nm. Continuous line represents amorphous state and dashed line, crystalline. (b) Reflectance spectrum for a  $\text{Sb}_2\text{S}_3$  layer on top of a gold grating with a period of 1550 nm, duty cycle 0.5, normal incidence, p-polarized light, Gaussian beam, a height of the grooves of 50 nm. The thickness of  $\text{Sb}_2\text{S}_3$  layer is 200 nm. Continuous line represents amorphous state and dashed line, crystalline.

Although calculations are shown here for  $\text{Sb}_2\text{S}_3$ , a similar behavior is found for other phase-change materials such as GaS after optimization of the PCM layer thickness to have a plasmon resonance at 1550 nm.

Another interesting configuration is that shown in Figure 23. In this case, only the grooves are metallic, generating a localized surface plasmon in each groove.<sup>29</sup> There is not a metallic layer under the grooves, and hence, the plasmon cannot travel. For this reason, a waveguide should be introduced. The coupling of all the LSPR can create a guided mode inside the waveguide, and light can travel through it. Depending on the phase of  $\text{Sb}_2\text{S}_3$ , LSPR are either generated or not, and consequently, a type of reconfigurable waveguide can be designed. In this configuration,  $\text{SiO}_2$  is used to reduce the index contrast between the waveguide and the incident medium.

From the numerical point of view, this case is more complicated than previous ones and, we are still analyzing it in order to improve reliability of results. The height of the grooves, the duty cycle, the period and the thickness of the waveguide need to be optimized for suitable performance.

This case, together with that shown in Fig. 22 are the most promising configurations and at present, they are being discussed in the consortium, in particular with partner NANOM-MEMS for developing detectors based on plasmon coupling through metallic gratings.



**Figure 23.** Scheme of a grating coupler based on gold grooves over a  $\text{Sb}_2\text{S}_3$  waveguide wrapped by  $\text{SiO}_2$ .

## 8. Cross-check with experimental data on plasmonic actuation

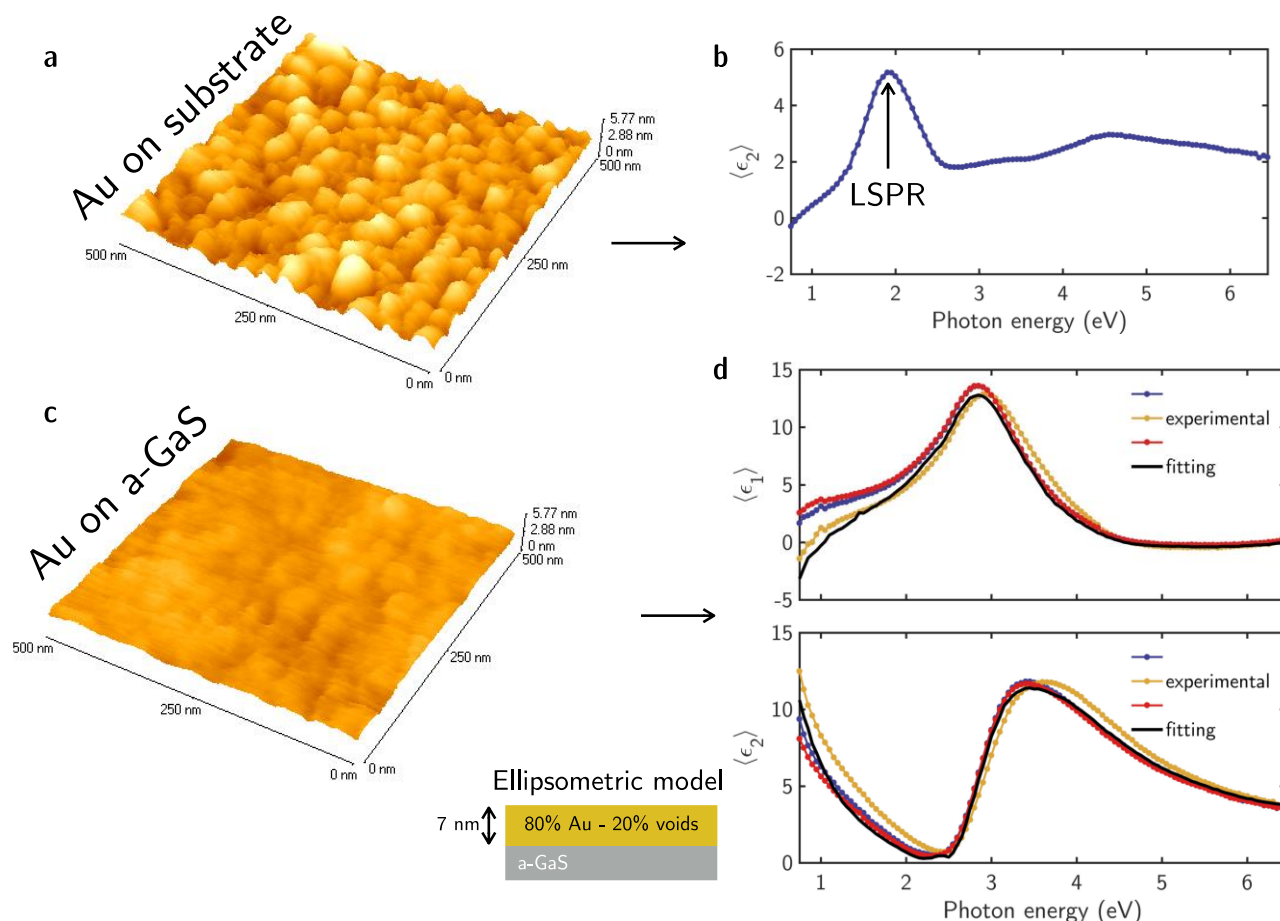
We turned our attention to technological issues linked to the fact that the most often used plasmonic materials, i.e., gold and silver, are both highly diffusive metals that could react with the PCM. Indeed, gold is known to diffuse readily into chalcogenides, and reacting forming alloying, for example, gold-sulfides, gold-tellurides, gold-selenides, and silver easily forms silver-sulfides, the latter known as silver tarnishing.

This reactivity leads to deleterious effects on plasmonic PCM structures, suppressing optical resonances and leading to changes in PCM switching properties (crystallization temperatures). Au and Ag diffusion, being a temperature-activated process, is also activated by the high-temperatures involved during the PCM phase-transformation process, e.g., during amorphization, the PCM must be heated above its melting temperature. Therefore, we have run in Task 2.2. some preliminary experiments of fabrication of plasmonic structures, coupling Au, Ag and Ga investigated in the previous sections with GaS and GaSe.

### I. Au NPs sputtered on amorphous GaS films grown by CVD

We sputtered Au NPs on an amorphous GaS samples grown by CVD at NANOTEC. As control, we deposited simultaneously the Au NPs on a dielectric sapphire substrate. The comparison of the AFM topography of the gold sputtered on the sapphire and on the amorphous GaS (a-GaS) shows completely different morphologies. Whereas the topography of the sputtered Au on the substrate shows clearly a uniform distribution of Au NPs (Figure 24a), the Au sputtered on the aGaS shows a flat morphology compatible with the formation of a very thin wetting layer (Figure 24c) instead of well shaped nanoparticles. As revealed optically by spectroscopic ellipsometry, Au NPs can support LSPRs at 1.8 eV compatible with the peak in the  $\langle\epsilon_2\rangle$  spectra at that same photon energy for the Au NPs on sapphire, as shown in Figure 24b. In order to gain a deeper understanding on the formation of this wetting Au layer on a-GaS, further ellipsometric analysis was performed. As shown as an inset in Figure 24d, the measured ellipsometric spectra of the sample can very well be fitted using a multilayer model consisting of a 7 nm Au layer on the a-GaS substrate.

**Therefore, sputtering Au NPs on a-GaS is not a feasible way to achieve a plasmonic actuation or coupling. This is due to the reactivity the Au NPs with the S-atoms of the chalcogenides causing the formation of a wetting thin layer instead of Au NPs and thus, inhibiting the LSPR excitation.**



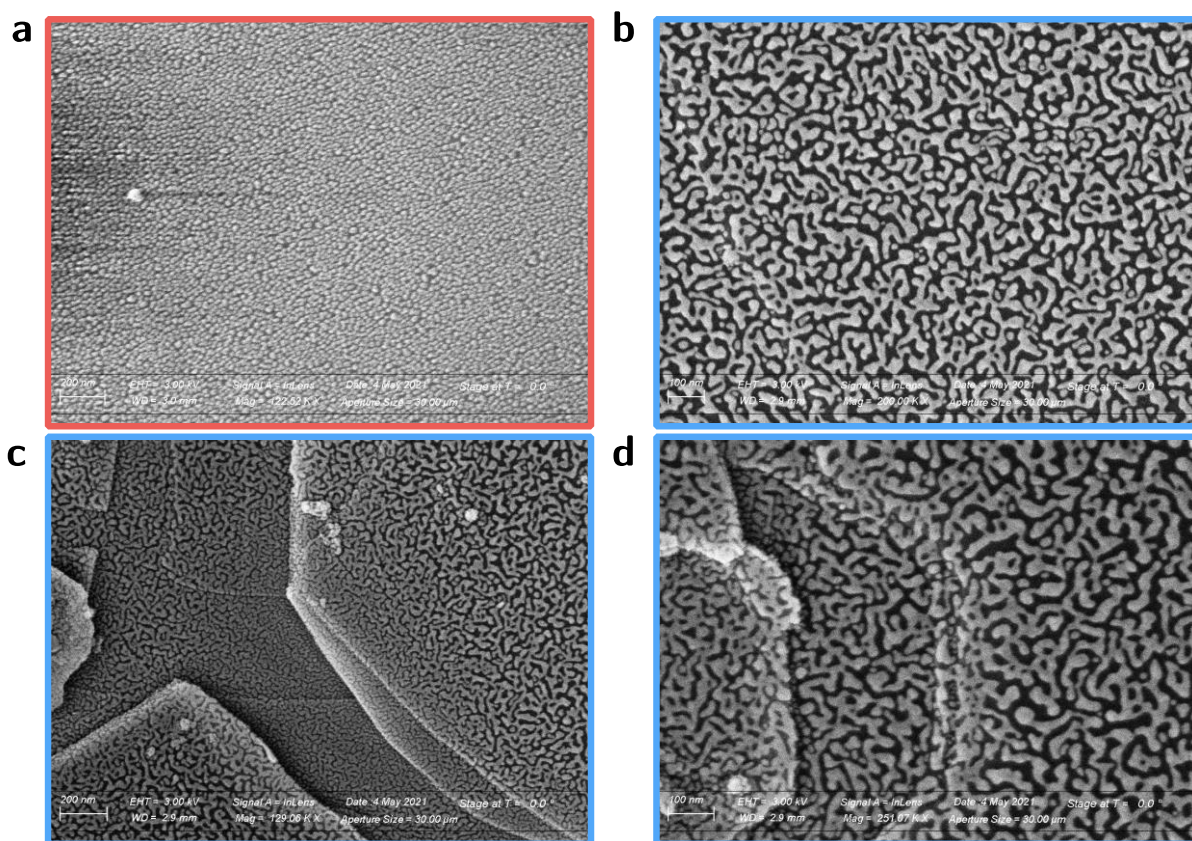
**Figure 24.** AFM topography of Au sputtered NPs on (a) a sapphire substrate and (b) CVD grown aGaS. (c) Imaginary part of the pseudo dielectric function measured on Au NPs sputtered on a sapphire substrate. (d) Complex pseudo dielectric function measured on Au NPs sputtered on a-GaS. The fitting of the experimental measurement was performed using the model indicated as an inset.

## II. Au NPs sputtered on crystalline exfoliated GaS flakes

Au NPs were also sputtered on mechanically exfoliated crystalline GaS on sapphire; this sample couples Au NPs to crystalline GaS to check if the problem of reactivity of Au with S-chalcogenide is for the amorphous phase materials or it applies also to crystalline materials.

As in the previous case, the Au NPs sputtered on the dielectric sapphire was used as control. The AuNPs/GaS(crystalline) samples show completely different morphology as revealed by the scanning electron microscopy images in Figure 25 from the AuNPs/sapphire control. The Au sputtered on sapphire shows a uniform distribution of NPs (Figure 25a). On the contrary, when analyzing the morphology of Au NPs sputtered on the crystalline GaS flake, we can appreciate a surface covered by uncoalesced islands. As seen in Figure 25b-d, this uncoalesced islands are evenly distributed on the stratified regions appearing due to the layered nature of GaS.





**Figure 25.** Scanning electron microscopy images of Au NPs sputtered on (a) the sapphire and on (b-d) the GaS crystalline flake (blue).

In order to investigate the optical response of these layer consisting on uncoalesced islands and how it compares to that of Au NPs, ellipsometric analysis of the sample has been performed. Figure 26a shows the imaginary part of the pseudodielectric function measured on the exfoliated crystalline GaS flakes before the Au sputtering process. The spectrum shows the characteristic critical points of GaS revealing the good crystalline quality of the exfoliated GaS samples. In that same Figure, it is shown the pseudodielectric function of the sputtered AuNPs on the sapphire substrate used as control. The peak at 2 eV corresponds to the LSPR of the Au NPs distribution formed on the dielectric sapphire substrate. Figure 26b shows the imaginary part of the pseudodielectric function of the Au sputtered on the exfoliated crystalline GaS. The spectrum shows two peaks at 3.9 eV and 5.6 eV attributed the critical points of GaS. The peak at 2.1 eV can be attributed to LSPRs excited by the uncoalesced Au islands.

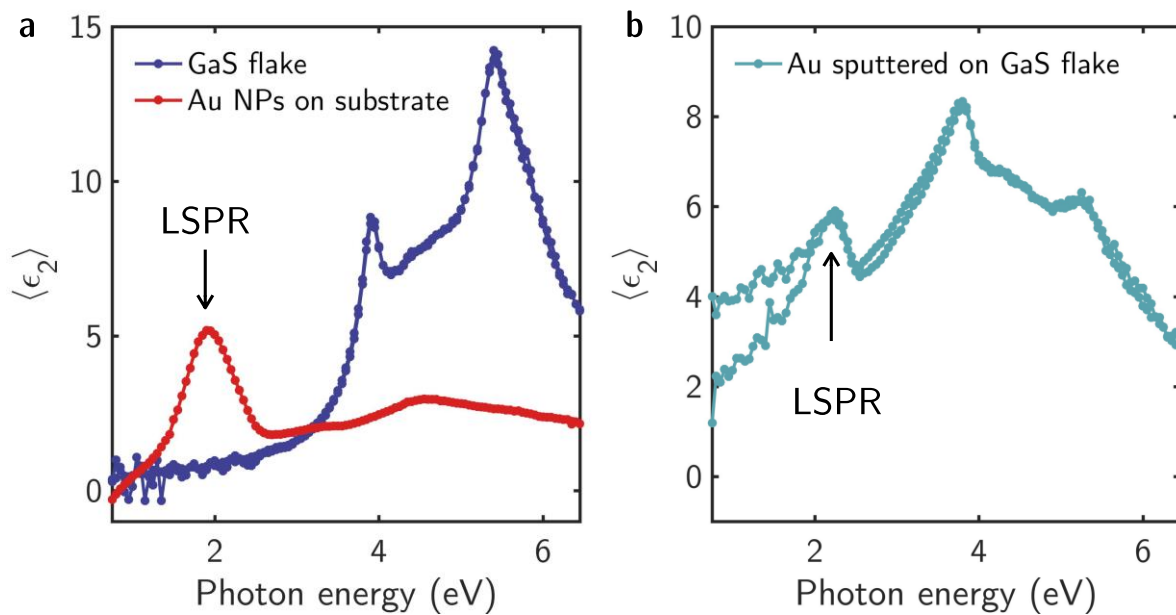
Although in principle this ensemble of irregular uncoalesced islands can support LSPRs, from the design and fabrication point of view can be problematic due to the difficulty in controlling the density and size of the islands, leading to uncontrolled plasmon resonance.

Thus, while for the Au NPs sputtered on amorphous a-GaS their LSPR is completely quenched, for the Au NPs on crystalline flakes their LSPR can be excited. This difference between the Au sputtered on amorphous and



crystalline GaS indicates a different aGaS /Au and crystalline GaS/Au interface energy that leads to a higher wetting of Au on amorphous GaS. Nevertheless, in both cases, the morphology of AuNPs on cannot be controlled inhibiting the practical exploitation of this process. Furthermore, the shape and distribution of those uncoalesced Au islands changes continuously during temperature variations for the amorphous-crystalline transformation leading to uncontrolled dynamics.

It is worth mentioning that the similar morphology of the Au layer was observed when sputtering Au NPs were sputtered on exfoliated crystalline GaSe.

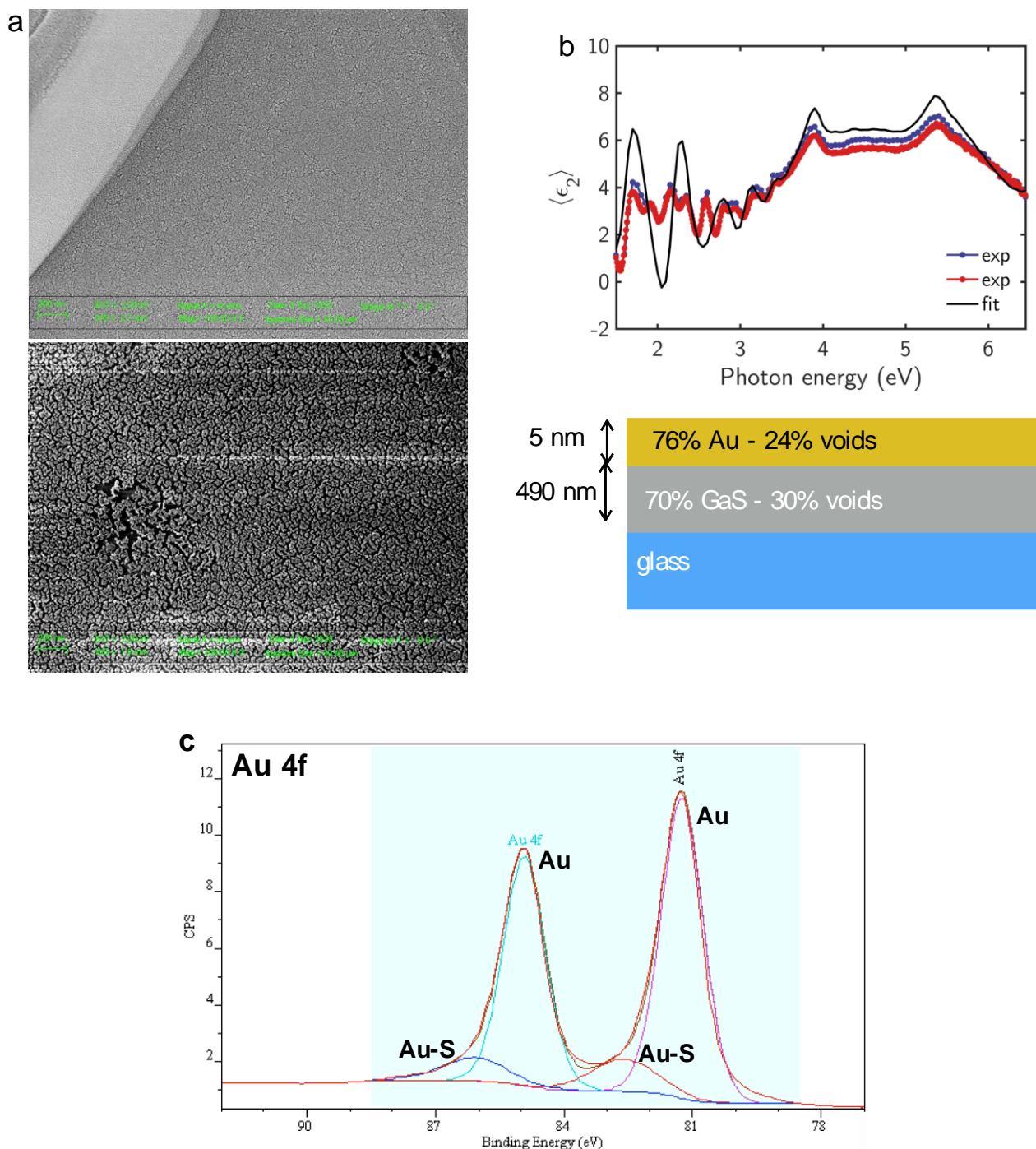


**Figure 26.** Imaginary part of the pseudodielectric function measured on (a) the exfoliated GaS before the Au sputtering and (b) on the Au NPs sputtered on the control sapphire substrate. (b) Imaginary part of the pseudodielectric function measured on the GaS flake after the Au NPs sputtering. With arrows are indicated the LSPR peaks of the sputtered Au nanoparticles/uncoalesced islands.

### III. Au NPs evaporated on exfoliated GaS flakes

In order to determine if the above reactivity of Au/GaS was a consequence of the ions present in the sputtering process, we also have explored evaporation of gold on exfoliated GaS flakes. Figure 27a shows the morphology of the Au layer as revealed by scanning electron microscopy. The evaporated Au layer is not continuous. Also in this case, an ensemble of uncoalesced Au islands covers the surface of the GaS flake, indicating that this kind of wetting layer is due to an intrinsic reactivity of the Au/GaS system, rather than coming from the Au deposition process. The spectroscopic analysis of the Au evaporated sample is shown in Figure 27b. The spectroscopic spectra could be fitted using a multilayer configuration in which a GaS layer with thickness  $\approx 500$  nm is covered by a 5 nm thick Au layer with a 24 % of voids. This void percentage represents the discontinuity in the Au layer. Chemical

analysis performed on the sample using X-ray photoelectron spectroscopy (XPS) is shown in Figure 27c. The fitting of the 4f photoelectron core level of Au reveals the reactivity of Au with the S dangling bonds of GaS to form Au-S bonds, demonstrating the reactivity of gold with chalcogenides.



**Figure 27.** (a) Scanning electron images of the surface the ultrathin Au layer evaporated on exfoliated GaS. (b) Pseudo dielectric function measured on the evaporated ultrathin Au layer on exfoliated GaS and scheme of the model used for the ellipsometric modelling. (c) XPS analysis of the 4f photoelectron core level of Au.

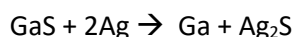
#### IV. Amorphous GaS deposited on Ag nanostructures

Silver (Ag) is another common metal used for plasmonic coupling. Therefore, experiments have been performed using silver as plasmonic material both as thin films and as bidimensional plasmonic metasurface arrangement (an Ag grating). The Ag metasurfaces has been designed to have a plasmon resonance that can couple light into the GaS bandgap energy. Specifically, the Ag substrate consist on two different parts as shown in Figure 28a:

- A thin Ag layer on a PET substrate;
- A nanopatterned array of PET cubes covered by an Ag layer creating a plasmonic metasurface.

The optical response of both systems was characterized before and after the a-GaS deposition using spectroscopic ellipsometry as shown in Figure 28b-e.

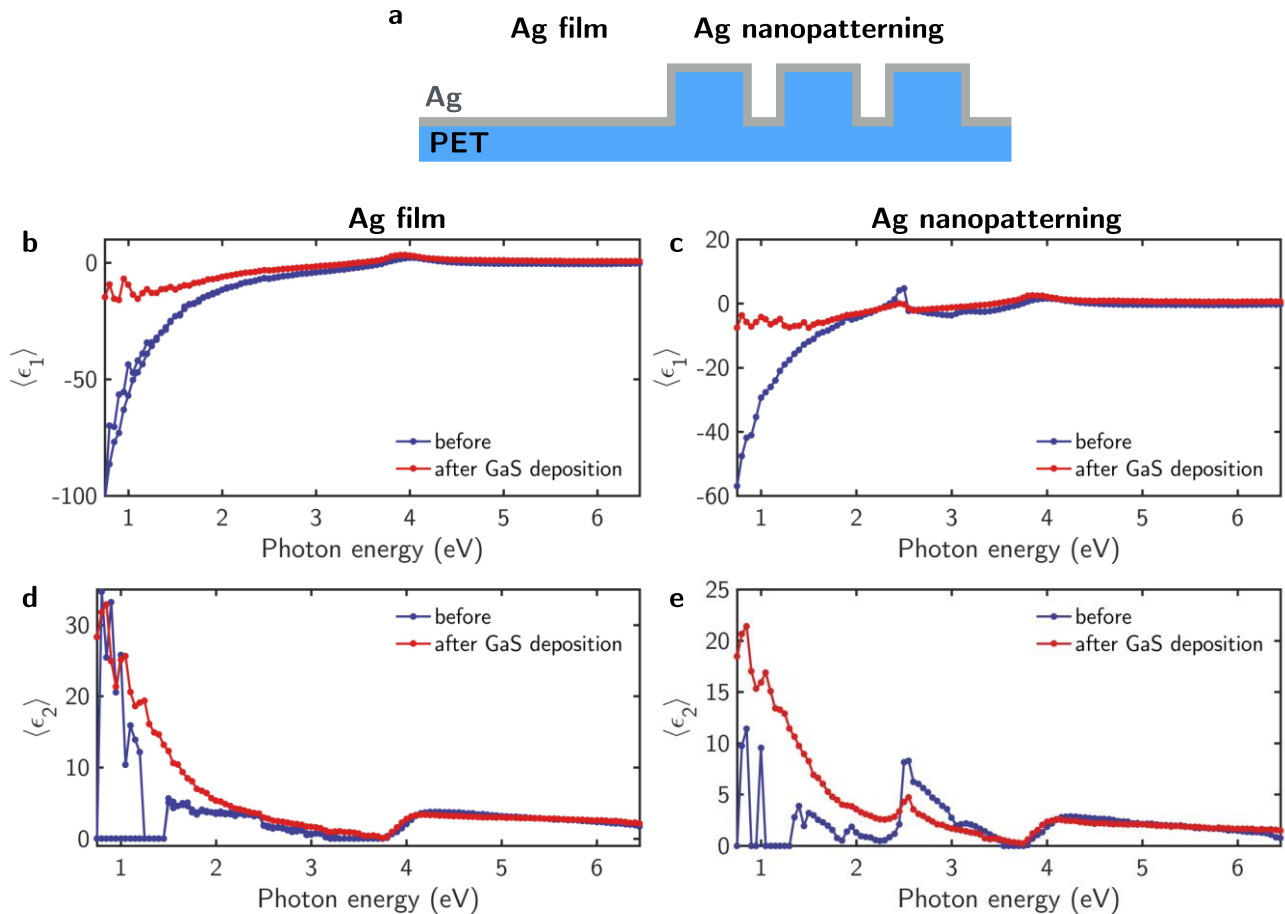
In the case of the Ag thin film on PET before the a-GaS deposition (blue line in Figure 28b,d), the pseudo dielectric function shows the characteristic Drude-like behavior of Ag below 3.5 eV and interband transitions above that photon energy. The values of  $\langle \epsilon_2 \rangle$  going to zero can be explained by light scattering due to the granular morphology of the Ag layer. When depositing the layer of a-GaS on top there of the Ag film, it can be seen in the  $\langle \epsilon_1 \rangle$  spectrum a quenching of the Drude component due to the transformation of Ag into silver sulfide  $\text{Ag}_2\text{S}$ , a phenomenon known as silver-tarnishing, leaving some gallium clusters according to the reaction:



For the nanopatterned region, before the aGaS deposition, the collective plasmonic response of the metasurface can be seen as a peak at 2.6 eV in the  $\langle \epsilon_2 \rangle$  spectra. After the deposition of the aGaS the plasmonic resonance of the system is quenched. This effect has also been observed by other authors working with Ag films and nanoparticles in sulfur rich environments.<sup>17,29</sup>

It is worth mentioning that during the Raman analysis of the aGaS photobleaching effects were encountered, burning the sample and making impossible its characterization even with  $\mu\text{W}$  laser powers. These effects are a direct consequence of the interaction of Ag with the GaS.

**On the basis of these preliminary experimental findings, we ruled out the possibility to use silver-based plasmonics and thermoplasmonics with chalcogenides PCMs.**



**Figure 28.** (a) Scheme of the Ag substrates consisting on: a thin Ag layer on a PET substrate; a nanopatterned array of PET cubes covered by an Ag layer creating a plasmonic metasurface. Complex pseudo dielectric function measured before and after the aGaS deposition on the (b,d) Ag thin film area and (c,e) nanopatterned area.

## 9. Identified solutions

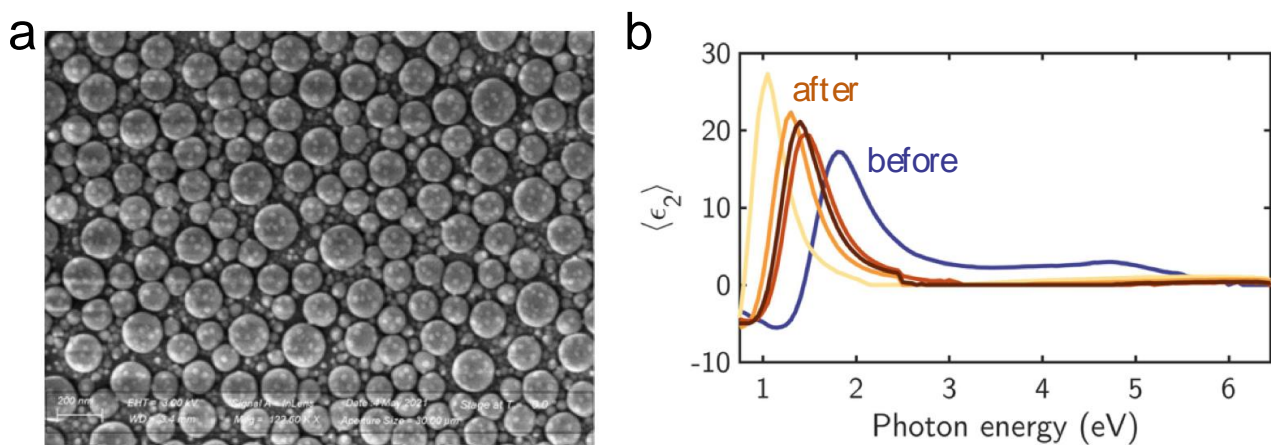
To counteract the large diffusivity of high-performing plasmon-supporting metals of gold and silver, a few strategies have been already identified.

A first approach to the problem of the reactivity of plasmonic metals is to search for alternative, non-reactive plasmonic metals. Any such options should ideally be CMOS-compatible, to allow for, ultimately, easy integration into PIC fabrication lines.

The identified option so far is based on plasmonic Ga nanoparticles, as simulated in previous sections of this deliverable, for the following reasons:

- 1) Gallium nanoparticle can be formed intrinsically during the growth of the chalcogenides, GaS, GaSe, GaTe without additional fabrication steps
- 2) Ga nanoparticles do not diffuse and interact with the chalcogenides. Their 1 nm ultrathin oxide layer act as a barrier that inhibit the interaction of Ga with S, Se and Te.
- 3) They are very stable with temperature up to 600°C; therefore, they are not modified during the crystallization and amorphization dynamics when temperature is varied.
- 4) Ga nanoantennas are stable to laser irradiation; hence, they can function during the cycling of the laser induced phase change.

So far, and as a proof to the stability of Ga NPs when compared to Au and Ag, CVD grown aGaS was deposited on GaS NPs. The morphology of the sample after deposition can be seen in Figure 29a. The scanning electron microscopy image of the sample after the aGaS deposition show how the GaNPs distribution and hemispherical shape is preserved. The ellipsometric analysis shown in Figure 29b reveals a red-shift of the LSPR peak of the Ga NPs after aGaS deposition. This behavior is consistent with the red-shift of LSPRs when surrounded by a higher refractive index medium (air vs aGaS).



**Figure 29.** (a) Scanning electron microscopy image of Ga NPs after deposition of CVD grown aGaS on top. (b) Imaginary part of the pseudo dielectric function measured on GaNPs before and after the deposition of CVD grown aGaS on top.

Another approach, if Au or Ag is required as plasmonic metal, is to place anti-diffusion barriers between the plasmonic material and the PCM. Of course, it is important that any such a diffusion barrier should not significantly alter, at least in a deleterious way, the optical or thermal properties of the device itself.

Staying in the 2D materials the best option is the transparent graphene, which can be deposited also at NANOTEC and can be exploited in this project creating novel PCMs/graphene heterojunctions.



## 10. Conclusions

We have analyzed various plasmonic metals coupled to chalcogenides PCM, aiming at using plasmonic electromagnetic actuation of the phase transformation of PCMs at optical frequencies, and at using thermoplasmonics for providing the heating needed for the thermal phase change actuation. We have also proposed and analyzed several configurations of plasmonic-PCM photodetectors. The preliminary simulations show that:

- 1) The geometry parameters or radius and interdistance of hemispherical dimer nanoantennas supported on PCMs have been investigated in order to control and tune their plasmonic resonance and match it to the laser wavelength used for activating phase transformation.
- 2) Several plasmonic metals have been compared for thermoplasmonics.
- 3) There is substantial reactivity when Ag, and Au plasmonic metals are directly interfaced with phase change chalcogenide layers. Diffusion occurs at room temperature and is accelerated when the phase change material is heated during the switching process. Our results show that Au and Ag react with chalcogenides and, therefore, should be avoided in tunable plasmonic device designs.
- 4) Ga dimer nanoantennas are a viable solution for coupling plasmonics and thermoplasmonics with chalcogenides PCMs.
- 5) Plasmonic-PCM based photodetectors based on plasmonic gratings can be realized using plasmonic configurations where the plasmon is excited at the metal-PCM interface.

The calculations presented in this deliverable are meant to be used as guideline for further development and optimization of plasmonic coupling to PCM, also in light of the PCMs that will be finally selected and optimized in the course of the project. Therefore, an updated of this deliverable will be released with the detailed simulations of the final selected plasmonic configurations for the demonstrators.

## 11. References

1. Maier, S. A. *Plasmonics: Fundamentals and applications. Plasmonics: Fundamentals and Applications* (2007). doi:10.1007/0-387-37825-1
2. Baffou, G. Thermoplasmonics: Heating metal nanoparticles using light. *Thermoplasmonics Heat. Met. Nanoparticles Using Light* 1–291 (2017). doi:10.1017/9781108289801
3. Wuttig, M. & Yamada, N. Phase-change materials for rewriteable data storage. *Nat. Mater.* **6**, 824–832 (2007).
4. Burr, G. W. *et al.* Phase change memory technology. *J. Vac. Sci. Technol. B, Nanotechnol. Microelectron. Mater. Process. Meas. Phenom.* **28**, 223–262 (2010).
5. Ovshinsky, S. R. Reversible electrical switching phenomena in disordered structures. *Phys. Rev. Lett.* **21**, 1450–1453 (1968).
6. Zhou, J. Tailoring geometric phases of two-dimensional functional materials under light: a brief review. *Int. J. Smart Nano Mater.* **11**, 191–206 (2020).
7. Haffner, C. *et al.* Low-loss plasmon-assisted electro-optic modulator. *Nature* **556**, 483–486 (2018).
8. Farmakidis, N. *et al.* Plasmonic nanogap enhanced phase-change devices with dual electrical-optical functionality. *Sci. Adv.* **5**, 1–8 (2019).
9. Alarreta, R. U. I. Z. D. E. G. *et al.* Plasmonically-enhanced all-optical integrated phase-change memory. **27**, 24724–24738 (2019).



10. Eggleton, B. J., Luther-Davies, B. & Richardson, K. Chalcogenide photonics. *Nat. Photonics* **5**, 141–148 (2011).
11. Gutiérrez, Y. *et al.* Gallium Polymorphs: Phase-Dependent Plasmonics. *Adv. Opt. Mater.* **7**, 1–10 (2019).
12. Gemo, E. *et al.* A plasmonically enhanced route to faster and more energy-efficient phase-change integrated photonic memory and computing devices. *J. Appl. Phys.* **129**, 110902 (2021).
13. LUMERICAL.
14. COMSOL.
15. Lalis, A., Tessier, G., Plain, J. & Baffou, G. Quantifying the Efficiency of Plasmonic Materials for Near-Field Enhancement and Photothermal Conversion. *J. Phys. Chem. C* **119**, 25518–25528 (2015).
16. McMahon, M. D., Lopez, R., Meyer, H. M., Feldman, L. C. & Haglund, R. F. Rapid tarnishing of silver nanoparticles in ambient laboratory air. *Appl. Phys. B Lasers Opt.* **80**, 915–921 (2005).
17. Oates, T. W. H., Losurdo, M., Noda, S. & Hinrichs, K. The effect of atmospheric tarnishing on the optical and structural properties of silver nanoparticles. *J. Phys. D. Appl. Phys.* **46**, 145308 (2013).
18. Sanz, J. M. *et al.* UV Plasmonic Behavior of Various Metal Nanoparticles in the Near- and Far-Field Regimes: Geometry and Substrate Effects. *J. Phys. Chem. C* **117**, 19606–19615 (2013).
19. Losurdo, M., Suvorova, A., Rubanov, S., Hingerl, K. & Brown, A. S. Thermally stable coexistence of liquid and solid phases in gallium nanoparticles. *Nat. Mater.* **15**, 995–1002 (2016).
20. Gutiérrez, Y. *et al.* Polymorphic gallium for active resonance tuning in photonic nanostructures: from bulk gallium to two-dimensional (2D) gallene. *Nanophotonics* **9**, 4233–4252 (2020).
21. Abdollahramezani, S. *et al.* Tunable nanophotonics enabled by chalcogenide phase-change materials. *Nanophotonics* **9**, 1189–1241 (2020).
22. Scholl, J. a, Koh, A. L. & Dionne, J. a. Quantum plasmon resonances of individual metallic nanoparticles. *Nature* **483**, 421–7 (2012).
23. Bohren, C. F. Absorption and scattering of light by small particles. *Absorpt. Scatt. Light by small Part.* (1983). doi:10.1088/0031-9112/35/3/025
24. Delaney, M., Zeimpekis, I., Lawson, D., Hewak, D. W. & Muskens, O. L. A New Family of Ultralow Loss Reversible Phase-Change Materials for Photonic Integrated Circuits: Sb<sub>2</sub>S<sub>3</sub> and Sb<sub>2</sub>Se<sub>3</sub>. *Adv. Funct. Mater.* **30**, 2002447 (2020).
25. Albella, P. *et al.* Shape matters: Plasmonic nanoparticle shape enhances interaction with dielectric substrate. *Nano Lett.* **11**, 3531–3537 (2011).
26. Ríos, C. *et al.* Integrated all-photonic non-volatile multi-level memory. *Nat. Photonics* **9**, 725–732 (2015).
27. Rechberger, W. *et al.* Optical properties of two interacting gold nanoparticles. *Opt. Commun.* **220**, 137–141 (2003).
28. Dong, W. *et al.* Wide Bandgap Phase Change Material Tuned Visible Photonics. *Adv. Funct. Mater.* **29**, 1806181 (2019).
29. Sinclair, J. D. Tarnishing of Silver by Organic Sulfur Vapors: Rates and Film Characteristics. *J. Electrochem. Soc.* **129**, 33–40 (1982).